1
Pharmacokinetics and Pharmacodynamics (PK/PD) of Bionanomaterials

Ergang Liu, Meng Zhang, and Yongzhuo Huang

COPYRIGHTED MATERIAL

1.1
Introduction

Nanomaterials (NMs) refer to synthetic or naturally occurring substances with size ranging from 1 to 1000 nm. The concept of "nanomaterial" was proposed by Feynman 50 years ago in the field of physics [1], which has since unveiled an era of nanotechnology. NMs contain merely tens to thousands of atoms, and are characterized by the surface and quantum size effects that are distinct from the bulk matters, and have thus gained wide applications in various areas [2]. For example, in medical application, nanotechnology has attracted specific attention in cancer therapy and diagnosis, largely due to the proposal of enhanced permeation and retention (EPR) effect by Maeda and coworkers; they demonstrated that nanosized macromolecules displayed a preferential retention in tumor site due to the leaky vasculatures [3, 4]. The EPR effect-associated nanomedicine composed of various natural or synthetic entities in the nanoscale, which have been developed to deliver drugs/imaging agents to the tumors based on the passive targeting effect [5]. Later, in order to further increase the transport efficiency, antibodies or targeting ligands with high binding affinity to tumor-overexpressed surface antigens or receptors have been applied to conjugate onto the surface of NMs to achieve the so-called active targeting [6].

NMs can also be applied in formulation development because of their capability to improve solubility [7], drug permeation [8], and drug stability [9]. Pharmaceutical nanotechnology may thus help improve druggability of those active molecules that are otherwise considered to be unsuitable for formulation development for clinical use due to unfavorable properties such as poor solubility and low permeation to the lipid bilayer membranes [10].

The emerging nanomedicine has greatly promoted drug development, and a good number of NM-based medicine or diagnostic agents have entered clinical trials, most in the field of cancer therapy, in which the NM-based delivery strategies are characterized by EPR effect for achieving tumor targeting. However, in spite of the enhanced permeability of the tumor vasculature, not all types of NMs

Biomedical Nanomaterials, First Edition. Edited by Yuliang Zhao and Youqing Shen.
© 2016 Wiley-VCH Verlag GmbH & Co. KGaA. Published 2016 by Wiley-VCH Verlag GmbH & Co. KGaA.

could benefit from EPR effect to achieve a substantial targeting efficiency [11]. The *in vivo* ADME (absorption, distribution, metabolism, and excretion) behaviors of NMs vary because of the difference of the surface properties, size, and charges of the NMs, as well as their compositions, often leading to inconsistent therapeutic outcomes in animal studies [12].

On this account, investigation of "what the body does to NMs" may help us with a better understanding of the *in vivo* fate. We herein present a brief introduction of the commonly utilized NMs in pharmaceutical research, the anatomic features of the body and tumor, and the physiochemical natures of NMs that affect the *in vivo* fate. The established PK/PD models for simulating the *in vivo* ADME behavior of NMs will also be introduced. We hope this summary would give a glimpse into the complicated *in vivo* processes and provide helpful information for the rational design of NM-based drug delivery systems.

1.2 Commonly Utilized NMs in Pharmaceutical Research

NMs can be categorized into different groups based on certain classification. To make it simple, we use the natural/synthetic classification in this chapter because the natural/synthetic NMs are generally disposed by the body in different ways. Moreover, inorganic NMs characterized by the hard-core structure bear unique physical characteristics (magnetism, thermal response to radiation, optical features, etc.) [13, 14], and are discussed as an independent section. Other resources such as cell-based NMs (e.g., RBCs [15] and MSCs [16]) and components from microbes (e.g., inactivated virus envelope [17] and TAT [18]), are usually utilized with preservation of their original natures, which are thereby discussed as a complimentary to this classification.

1.2.1 Natural NMs

Natural NMs have been widely investigated because of their biodegradability and compatibility to human body. As known, lipids, proteins, carbohydrates, and nucleic acids are highly biodegradable in the body. Phospholipids are one of the most widely applied natural resources to build the nanocarriers such as liposomes and solid lipid nanoparticles (SLNs) [19]. Polysaccharides, including a variety of carbohydrates with different structures and functional groups, can be utilized to build different types of nanoparticles. Protein-based NMs (typically, serum proteins such as albumin [20], high-density lipoprotein (HDL) [21], and lactoferrin [22]) are often utilized as drug carriers.

1.2.1.1 Lipid-Based NMs

Lipid-based NMs include liposomes [19], SLNs, micelles [23], and nanoemulsions [24] (Figure 1.1). The main components of liposomes are phospholipids. In aqueous solution, the phospholipids will self-assemble into a bilayer structure

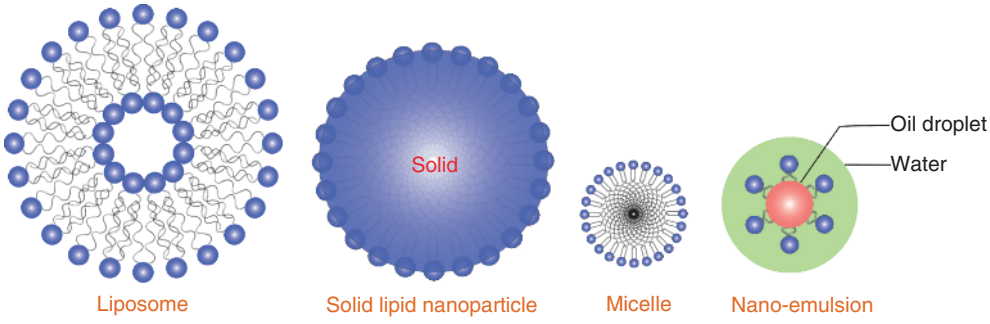

Figure 1.1 Schematic illustration of lipid-based NMs.

that functions as drug carriers with hydrophilic drugs encapsulated inside the interior, whereas hydrophobic drugs in bilayer [19]. One-tail lipids are inclined to form micelles in aqueous media [25], whereas using steric acid or oleic acid supplemented with surfactants to stabilize the solid/liquid lipids normally results in nanoparticles [26] or emulsions [27].

1.2.1.2 Protein-Based NMs

Protein-based drug carriers have been widely used in pharmaceutical industry. However, owing to the concerns of protein immunogenicity (e.g., OVA, which has been utilized as adjuvant for immune activation [28]), endogenous serum-rich proteins with low immunogenicity and long half-life such as albumin, high-density lipoprotein, and lactoferrin have distinct advantages [20–22]. As a case in point, albumin-bound paclitaxel nanoparticles (Abraxane®) have attained great market success [29]. In general, proteins can either be processed to form nanoparticles [30] or directly coupled with drugs by physical adsorption or via covalent bonds [20]. In certain instances, the protein carriers are further modified with targeting ligands to achieve specific delivery [31].

1.2.1.3 Polysaccharide-Based NMs

Polysaccharides originate from animal, plant, or bacterial sources. In general, the physicochemical properties of polysaccharides are governed by monosaccharide unit and the overall molecular weight [32]. The high molecular weight molecules, such as heparin and hyaluronic acid, show strong affinity to water molecules, and thus form hydrogels that have been widely applied for local administration because of their biocompatibility and sustained drug release functions [33]. The ionic polysaccharides can bind with molecules of the opposite charge, and the interaction normally leads to decreased solubility and the formation of nanoparticles [34].

1.2.2 Synthetic NMs

Although NMs based on naturally occurring materials have the advantages of biocompatibility and wide availability, structure modification is difficult

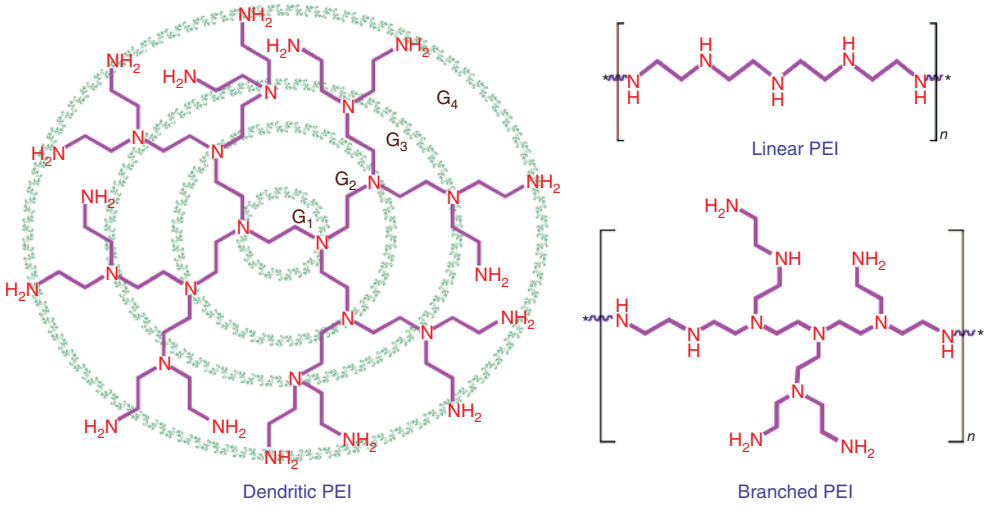

Figure 1.2 Various forms of PEI.

to process to tailor their functions to satisfy the needs from pharmaceutical application.

By contrast, synthetic polymers can be much more flexibly designed for a specific application. For example, by using the pH-sensitive synthetic materials, the NMs could release drugs in a pH-dependent manner for achieving tumor-targeting delivery [35], because the rapidly prolific neoplastic tissues normally secrete more lactose from the hyperactive anaerobic glycolysis, leading to a decreased pH in tumor microenvironment [36].

1.2.2.1 Diversity of Synthetic NMs in Forms

Synthetic NMs can be tailored for different purposes. For instance, polyethyleneimine (PEI) can be synthesized in the forms of linear, branched, or dendritic structures (Figure 1.2) [37]. Synthetic polymers can be fabricated into various types of NMs such as nanoparticles, micelles, and nanocubes. For example, poly(lactic-*co*-glycolic acid) (PLGA) can be made into widely applied nanoparticles [38], microspheres [39], and micelles [40].

NMs are often used as carriers for small molecular drugs. Drugs are loaded into NMs by encapsulation or via a covalent linkage, in order to improve the PK profiles and achieve targeting delivery to a specific site.

1.2.2.2 Drug Release Behaviors

Drug release from NMs is governed by the physiochemical properties of the drug and NMs. Burst release is often seen for the hydrophobic drugs in capsulation by liposomes, while sustained release for the hydrophilic drugs in liposomes, which are slow to diffuse across the lipid bilayers [41]. However, it is more complex to

investigate the drug release profile when NMs are injected to the body, and knowledge of the *in vitro in vivo* correlation (IVIVC) is still insufficient.

In order to reduce the unwanted drug exposure, a number of strategies have been developed to achieve a site-specific release of the loaded cargos.

pH-sensitive NMs

The slightly acidic tumor environment and endosome's even lower pH have attracted extensive interests in the application for designing NMs with the ability to respond to pH changes during the delivery. This strategy has been intensively explored by employing the polycationic dendrimers such as PEI and PAMAM. Acidic pH could cause the electrostatic repulsions between side chains in these polyamines because of the protonation of amino groups. As a result, the dendrimers swell in response to the acidic condition and the abrupt pH drop – the so-called "proton sponge" effect [42]. After engulfed by the cells, the swelling of NMs can lead to endosome rupture, and thus is favorable for intracellular drug release.

Another strategy is to use pH-sensitive linkage (e.g., hydrazone bonds) for cross-linking and building the NMs [43]. The NMs disassemble in a pH-dependent pattern, thus triggering drug release in acidic environments.

Redox-sensitive NMs

Besides the decreased pH, the rapidly growing tumor is also characterized by the intracellular reducibility due to the increased level of glutathione (GSH) [42]. The redox-sensitive NMs (e.g., NMs built via disulfide linkage) can display an accelerated drug release once entering the tumor cells.

Enzyme-sensitive NMs

Tumor-associated proteases have been widely investigated for their application as biomarkers in cancer diagnosis, prognosis, and therapy. Overexpression of tumor-associated proteases (e.g., MMP-2 [44], MMP-9 [45], and legumain [46]) in tumors provides ideal targets for the design of "smart" NMs with controlled release. A general strategy is to use a specific substrate peptide to modify the NMs, and the cleavage of the peptide would trigger drug release or cellular uptake.

Thermo/radio wave-sensitive NMs

Other stimulus-responsive NMs can respond to external physical stimulation (such as localized heating and electromagnetic radiation) and have been applied in drug delivery [47]. Specificity of this strategy is largely dependent on the precise control of the applied stimuli at the target sites.

1.2.3 Inorganic NMs

Inorganic NMs are distinguished from the organic NMs (soft matters) with the hard cores. In order to avoid aggregation in aqueous media, the inorganic cores are typically modified with surfactants or hydrophilic polymers to form a core – shell structure [48]. Of note, the *in vivo* biofate of inorganic NMs is greatly affected by the surface characteristics of the coating materials [49].

Inorganic NMs exhibit many unique physical properties – for example – fluorescence (quantum dots), superparamagnetism (iron oxide nanoparticles), photothermal effect (gold nanorods, carbon nanotubes), or special optical properties (silver nanoparticles) [13, 50]. These properties of the inorganic NMs have been utilized in cancer diagnosis and treatment applications.

1.2.4
Other NMs

Together with the rapid development of NMs, knowledge of NMs has accumulated. Proteins, in terms of the size, can also be viewed as bionanomaterials, which are rich in the body. As a case in point, albumin (MW 67 kDa) with a diameter around 7 nm [51] can serve as a unique "protein carrier" for drugs. Another example is the red blood cells (RBCs), with diameter from several to tens of micrometers [15], which may be regarded as a type of "microliposomes" to deliver therapeutic macromolecules. Moreover, even the protein capsids of a virus (size <100 nm) can be used as a "nanocapsule" [52]. Inspired by biomimetics, these physiologically originated NMs have been explored as novel carriers for drug delivery.

Moreover, there is another form of nanodrugs – the nanocrystals of hydrophobic drugs [53]. Such nanodosage forms can solve the solubility problem, and furthermore improve the PK profiles.

1.3
In vivo Biodistribution and the Evolving Targeting Principles for NMs

The targeting strategies have been mostly employed in cancer therapy areas. In general, there are two types of targeting strategies: the passive targeting via EPR effect and the active targeting mediated by antibodies or ligands that can specifically bind with receptors on cancer cells. Recently, with the growing knowledge of tumor physiology, the tumor microenvironments (e.g., acidic pH and the overexpressed proteases) have been used as a target for cancer drug delivery [6]. A combination of the targeting strategies by using multifunctional NMs has also been investigated for achieving improved specific targeted delivery and controlled release [54]. The ultimate goal is to increase drug concentration in tumor while reducing its exposure to the healthy organs.

1.3.1
Organ Distribution versus Cell-Specific Targeting

Ideally, NMs should be able to deliver the cargo drugs specifically into a target site. The *in vivo* fate of NMs is determined by a combination of multiple factors, including particle size, shape, and surface characteristics [55]. It is thus difficult to assess the overall targeting efficiency from *in vitro* data (e.g., cellular uptake by a

target cell line) for a given NM. A biodistribution study of the NMs is necessary to investigate the preferential accumulation site of the administrated NMs. If a certain NM is highly accumulated in a specific organ, it could be used as a potential drug carrier for targeting the organ.

However, organ-specific accumulation may not ensure the satisfactory treatment outcomes. For example, in brain cancer, an ideal delivery should be a "dual-targeting" mode, that is, the chemotherapeutics could not only preferentially accumulate in brain, but also selectively act on the cancer cells, while sparing the normal cells in the central nervous system and thus preventing adverse effects.

1.3.2 Targeting Delivery Strategies

With growing understanding of the pathology and diseases, different targeting strategies have been developed.

Passive targeting

EPR effect is one of the major mechanisms responsible for cancer nanomedicine. However, due to nonspecific capture by the RES and retention by organs such as liver, spleen, and lung, the vast majority (>95%) of administered nanomedicine distributes into the undesired organs [56]. The overall benefit of the targeting efficiency by EPR effect for clinical use is still not clear [57]. Much effort has been made on surface modification with hydrophilic polymers such as PEG to evade the RES uptake [58]. Furthermore, the extended blood circulation facilitates extravasation for increased tumor accumulation.

Targeting to membrane-overexpressed receptors

Many diseases are related to gene mutations that generally lead to phenotypic changes and overexpression of certain membrane receptors. The overexpressed membrane receptors may serve as "zip code" and facilitate site-specific drug delivery. The drug carriers modified with targeting ligands (e.g., antibody and peptide), like "postmen," would recognize the "address" and achieve precise delivery. Moreover, some receptors can also induce receptor-mediated endocytosis after binding [59]. An ideal targeting receptor should be specifically expressed in the pathological site, but does not exist in normal tissues or cells.

Tumor-overexpressed enzyme-mediated targeting

Tumor-overexpressed enzymes provide another group of promising targets for site-specific drug release. A typical design is that drugs are cross-linked with NMs by peptide substitutes, or encapsulated into NMs that are featured by the protease-triggered cell penetration, thus achieving tumor-specific drug release or cell entry. Furthermore, if the fluorochrome is linked with its quencher by using a protease substrate peptide, FRET (fluorescence resonance energy transfer) effect can be produced, leading to fluorescence quench. Such type of FRET-based probe can be specifically

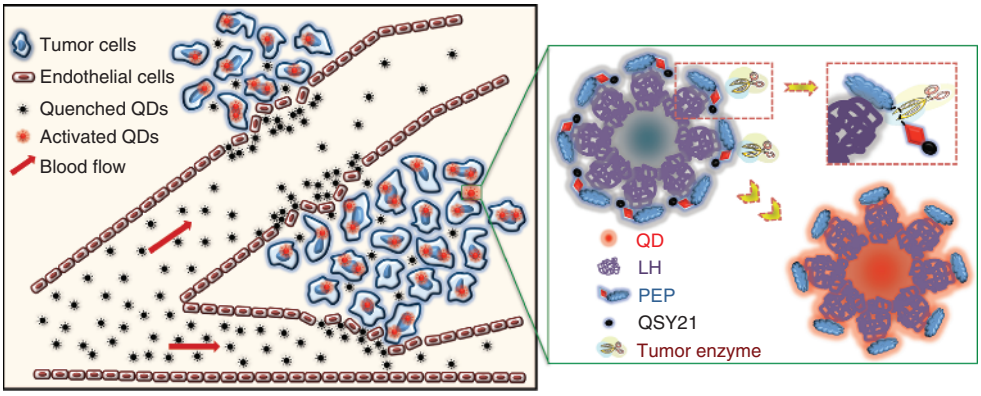

Figure 1.3 Schematic illustrations of activatable nanoprobe. The nanoprobe comprises two components (the fluorescence donor QD-LH and the FRET quencher QSY21), which are cross-linked via a chimeric peptide comprising LP and a legumain-cleavable sequence [60]. (Reprinted with permissions from John Wiley & Sons, Copyright 2014.)

activated by the tumor-overexpressed proteases, and thus serve as a potential method for tumor detection and imaging (Figure 1.3) [60].

Tumor microenvironment-responsive NMs

The slightly acidic tumor microenvironment [36] and high level of GSH [61] have been extensively explored for controlled drug release. For example, amphoteric polymers are neutral or negatively charged at pH 7.4, but become positively charged at slightly acidic condition [62]. The charge conversion facilitates NMs to be preferentially engulfed by the tumor cells because of the lowered extracellular pH in tumor tissue.

High level of GSH in cancer cells is the key factor for reduction-responsive drug delivery. For example, NMs that are built via disulfide bond can disassemble when exposed to the increased intracellular GSH, leading to burst release of the encapsulated drugs. Another interesting application is the cell-penetrating peptide (CPP)-mediated intracellular drug delivery. CPPs are effective in transporting macromolecules across the cellular membranes, but the delivery through the cell membrane could be an in-and-out bidirectional pattern [63]. The potential solution to entrap the cargo drugs inside the cytoplasm is to conjugate CPP with the drugs via disulfide bond. Once the linker is cleaved in the presence of high level of intracellular GSH, the cargo drugs will thus be left in the cytoplasm [15].

Physical targeting

The superparamagnetism of iron oxide nanoparticles with size of 3–50 nm has been applied for magnetic targeted drug delivery. In this strategy, drugs are normally encapsulated in the coating layers on the magnetic cores, or cross-linked onto the surface of the NMs [64].

In addition, photothermal effects of gold NMs have been explored for thermal-triggered drug release at the target site. For instance, gold

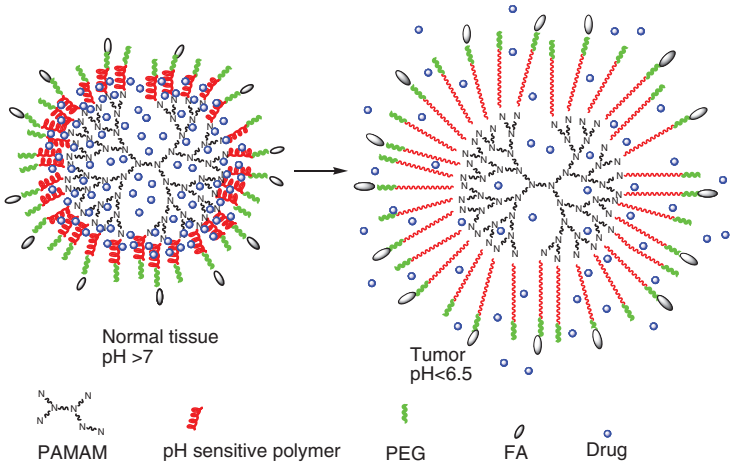

Figure 1.4 Schematic illustration of folate-modified pH-sensitive PAMAM. (Reprinted with permissions from Elsevier, Copyright 2012.)

nanorods are coated with a thermal sensitive layer, which could be degraded by heating of the inorganic cores under external light radiation [65].

Physical targeting delivery could be relatively precisely controlled by fine-tuning the external stimulations. However, there is still much room to improve for the precise focus of the external energy on the target sites.

Combination of different targeting strategies to achieve a "smart delivery"

The different targeting strategies can be combined to prepare the "smart" NMs by taking advantage of multiple characteristics of the tumor microenvironment to achieve a synergetic effect of drug delivery. For example, the pH-sensitive NMs can be further modified with a targeting moiety. It has been reported that a multifunctional drug delivery system was developed for enhanced tumor targeting via multiple mechanisms: (1) acidic microenvironment-triggered drug release, (2) folate modification for receptor-mediated active targeting, and (3) PEGylation-induced long circulation for passive targeting through EPR effect (Figure 1.4) [66].

1.4 Processing NMs by the Biological Systems

The body has evolved with a conservative mechanism of dealing with the biological "invaders" [67]: first, the circulating NMs will encounter serum proteins that tend to bind on to the surface of NMs and form a protein "corona" [68], and thus be identified and captured by the circulating leukocytes [69]; second, the majority of the circulating NMs will be trapped by RES organs and kidneys with fenestrated vasculatures, resulting in macrophage-mediated metabolism or renal

excretion [55]; third, the remaining NMs that survive from blood clearance will gain a chance to reach the target organs, where the retaining NMs will degrade, with drugs releasing into the extracellular space and releasing to the cells [70]. Therefore, once entering the blood circulation, NMs overcome multiple physiological barriers before reaching their target cells or subcellular organelles.

1.4.1 Anatomic Basis of NMs' *in vivo* Biodistribution Behavior

EPR effect is the important physiological basis for NMs' application in tumor. Anatomically, the neovasculatures in rapidly growing tumor are impaired with endothelial cells, thus generating nanosized gaps (400–600 nm) [71]. The leaky vessels facilitate extravasation of NMs to the tumor site [72]. Besides, the tumors overexpress a number of membrane receptors such as EGFRs [73], $\alpha_\gamma\beta_3$ integrin receptor [74], HER-2 [73], folate receptor [75], and transferrin receptor [76], which have been applied for mediating active targeting via interactions with the ligand-modified NMs and triggering receptor-induced endocytosis of NMs. By contrast, some overexpressed membrane proteins, such as CD-20 that not induce endocytosis [77], are less frequently used for targeting delivery. Moreover, the tumor-overexpressed enzymes, such as legumain, MMPs, and hyaluronidase [78], can serve as the stimulus factors for the enzyme-sensitive NMs with controlled release behavior.

However, the overall transport efficiency to tumor via blood circulation is still below satisfaction, because the majority of the circulating NMs is retained by other organs [79]. A better anatomical understanding of *in vivo* procession of NMs will be helpful for rational design of a highly efficient system.

In blood circulation, interactions between NMs and blood cells and serum proteins greatly affect the biofate of the circulating NMs. The composition of the "protein corona" on the NMs is determined by the protein/NM binding affinity and regional concentrations of the proteins [80]. Albumin, lipoprotein, and complements are the major constitutions of the "corona." Nevertheless, the protein absorption is a competitive process, and the difference in the composition leads to different biofate of the NMs [81]. Albumin is the most abundant serum protein with a plasma half-life of about 19–22 days. Albumin absorption onto the surface of NMs will prevent from further interaction with other types of proteins, and benefit prolonged circulation. On the contrary, the lipoprotein-bound NMs tend to accumulate in the tissues rich in lipoprotein receptors, while for example, albumin binding with complements usually induces clearance by the macrophages [81].

Tissues and organs serve as "filters," playing important roles in drug retention and metabolism as well (Figure 1.5). Due to anatomic differences (e.g., blood perfusion rate, vascular structure, and resident macrophage density), the tissues process the NMs in different mechanisms [81]. For example, the RES organs (e.g., liver, spleen, and the lung) with rich blood flow are the traps for NMs, where about 90–95% of the injected NMs are accumulated and metabolized [82]. Other

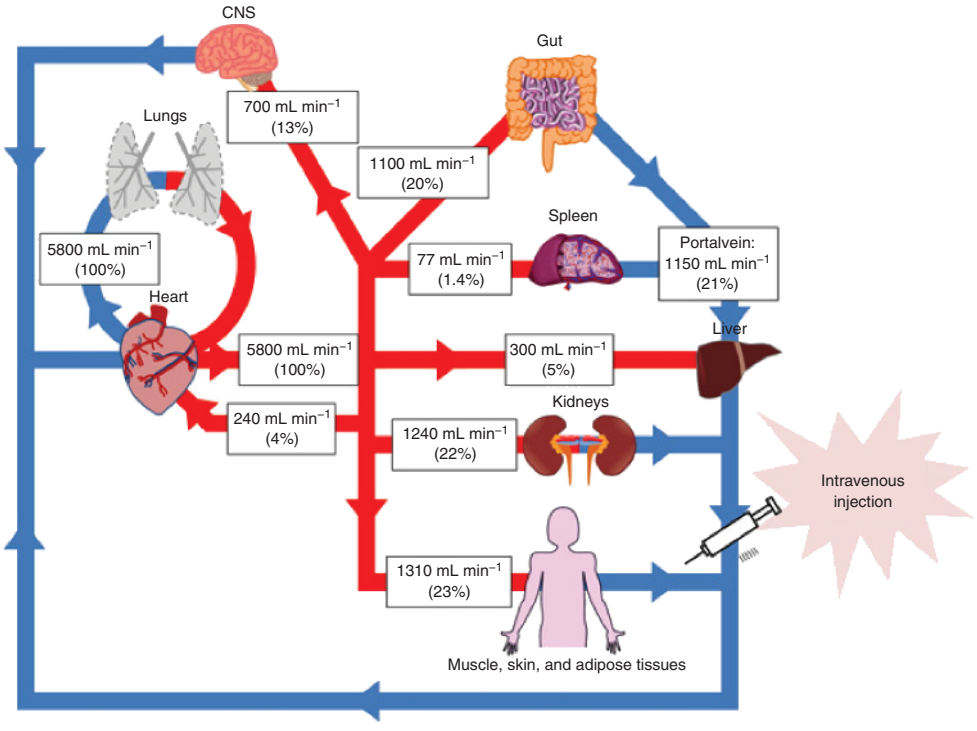

Figure 1.5 Distribution of blood flow in the pulmonary and systemic circulations [81]. (Reprinted with permissions from Elsevier, Copyright 2012.)

organs with rich blood flow such as heart and brain, on the contrary, do not show significant retention of the NMs, because of the rapid blood perfusion or tight junctions of the vasculature [83].

1.4.2 Factors Affecting *in vivo* Biodistribution of NMs

1.4.2.1 Size

The "filtration efficiency" in various organs is closely associated with the "cutoff size" of NMs (Figure 1.6). As for the liver, the size of the endothelial fenestrated capillaries ranges from 100 to 200 nm, and inside the sinusoid capillaries they are rich in kupffer cells that account for 80–90% of the body's resident macrophages with [81]. Therefore, the NMs size 100–200 nm will be engulfed by the sinusoidal resident macrophages; the spleen is apt to entrap the NMs larger than 200 nm due to the existence of discontinuous arterioles [84]. Although vascular pores of the lungs restrain extravasation of NMs larger than 3 nm, NM aggregates or large particles could be easily captured by the lungs in the extremely small diameter of the capillaries (3–13 μm) [81].

Tight junctions of renal basal lamina only allow the NMs smaller than 5 nm to pass through and be eliminated via urine [81].

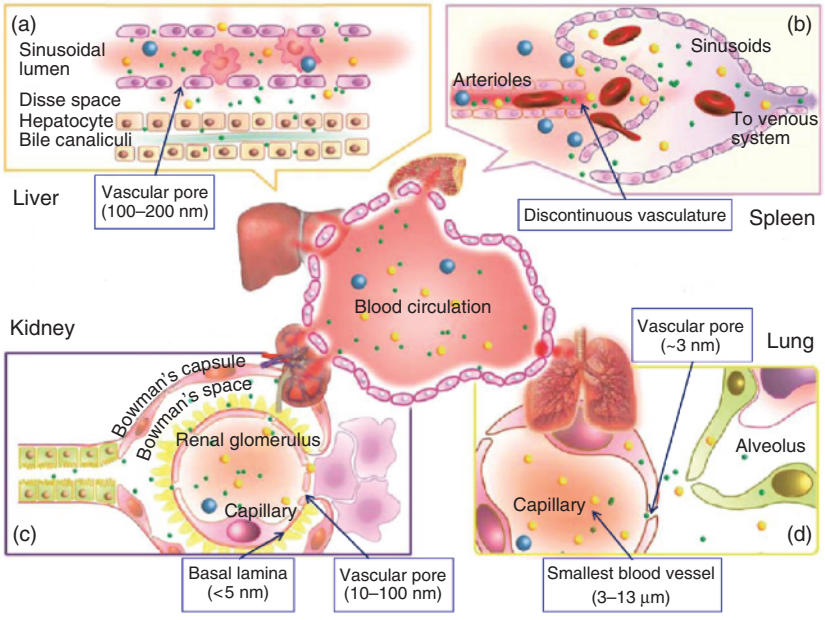

Figure 1.6 The tissue-specific extravasation of NMs [84]. (Reproduced with permission from American Chemical Society, Copyright 2012.)

1.4.2.2 Zeta Potential

Highly charged NMs tend to remain stable in aqueous solutions due to electrostatic repulsions [85]. Positively charged NMs are not compatible with the biological environments due to their strong interactions with cell membranes, serum proteins, and the complements that mediate endocytosis by mononuclear phagocytic system (MPS) [86]. In comparison, even though negative charge may also promote complement activation, the weak interaction with serum proteins and cell membranes may contribute to prolonged circulation; for instance, the reduced filtration by the glomerular basal membrane bearing anionic charges leads to slow renal clearance [87]. Compared with the charged NMs, neutral NMs display good compatibility to the body environment, and benefit long circulation, but once they aggregate, significant uptake by the lung and spleen occurs [88].

1.4.2.3 Shape and Deformability

The effects of shape on blood circulation are primarily determined by the aspect ratios of the NMs. Although elongated NMs are unfavorable for the interactions with plasma membrane, high aspect ratios may hinder membrane spreading during endocytosis, leading to inefficiently phagocytized by MPS. On the contrary, NMs with low aspect ratio have a more rapid clearance rate [89].

Deformability is another important factor that affects the *in vivo* biofate of the NMs. As a case in point, the RBCs may squeeze through the capillaries that are 25% smaller than their size, due to the deformability [90].

1.4.2.4 Hydrophilicity and Hydrophobicity

Hydrophilicity and hydrophobicity also greatly affect the NMs' pharmacokinetic behaviors [91]. In the physiological fluids, the hydrophobic NMs show high affinity to the nonpolar domains of the plasma proteins, promoting opsonization and leading to the decreased circulation time. Therefore, surface modification with hydrophilic polymers is a useful strategy for improving the stability and PK profiles of the hydrophobic NMs.

1.4.3 Metabolism and Elimination of NMs

1.4.3.1 Common Metabolism

The different biodistribution and disposition of the NMs will lead to different metabolism in the body. In general, the majority of the administrated NMs are captured by the RES organs, where the tissue-resident macrophages serve as the scavenger for degradation and clearance of the NMs. Apart from leukocyte-mediated clearance, superfine NMs and the degraded debris of NMs with size smaller than 5 nm will be excreted by the kidney; and the liver-accumulated NMs will be partially processed in the biliary pathway and excreted via feces [92].

1.4.3.2 Degradable versus Nondegradable NMs

Degradable NMs have been well accepted in drug delivery because of their biocompatibility, and nondegradable, inorganic NMs also have been applied with benefits of stability and robustness in resisting to enzyme digestion. However, it is a potential risk that nondegradable NMs may retain in the body for months, and the NMs that are deposited in the host organs may be released and lead to redistribution [93]. There are unknown threats about the excessive exposure of the NMs to the major organs such as the brain and heart. Therefore, the long-term nanotoxicity should be placed under scrutiny.

1.4.3.3 Free Drug versus Drug Encapsulated by NMs

Once encapsulated by NMs, the metabolism and elimination of drugs change, together with the altered biodistribution of NMs into different target organs. The drug-loaded NMs are apt to accumulate in macrophages, which express low level of drug metabolic enzymes [94], thereby potentially leading to a decreased rate of drug metabolism. On the contrary, the activities of the enzymes may be up- or downregulated by the NMs, giving rise to diverse effect on metabolism of the released drugs [95].

1.5 Rational Design of Long-Circulating NMs

In the body, MPS serves as scavenger to clear up the circulating exogenous particles. This self-protection nature, meanwhile, creates an extra barrier against

effective drug delivery by using the NM carriers. In fact, the drug delivery efficiency mediated by NMs is often under expectation, because the majority of the administrated NMs are entrapped in the undesired organs, leading to a rapid clearance from blood. The off-target effect raises side-toxicity concerns.

In order to address this problem, a number of methods have been investigated to reduce nonspecific retention by the RES, extend circulation time, and improve the delivery efficiency.

1.5.1 NMs with Optimal Physicochemical Characters

The nanosized entities should be built with optimal physicochemical parameters such as size, zeta potential, and shape, to achieve long circulation.

In general, superfine NMs less than 5 nm, or the nanoparticles with a size range of 10–20 nm, are disadvantageous for long circulation due to the potentially rapid renal excretion or hepatic uptake. However, if the NMs are designed to deliver drugs across capillaries with tight junctions such as the blood–brain barrier, where the gaps between endothelial cells are estimated to be less than 3 kDa (2.3 nm) [83], the superfine nanoparticles would have advantages. Usually, NMs between 20 and 200 nm have been mostly applied because of decreased hepatic retention.

The shape of the NMs should be tailored to achieve an extended circulation. For example, their shape significantly affects the interaction of NMs with the vessel wall. The nanorods, compared with nanospheres, may have a higher chance of binding with the wall due to larger length and tumbling motion [96]. The larger contact area usually produces stronger adhesion to the wall, displaying higher resistance to blood perfusion.

1.5.2 Surface Modification to Improve the Intrinsic Features of NMs

Surface modification plays an important role in determining the *in vivo* fate of the NMs, because it changes the physical characters of NMs such as size, zeta potential, and the bind affinity to plasma proteins [49].

PEGylation is the most commonly used method for surface modification of NMs. The coated hydrophilic and flexible PEG chains protect the NMs from adsorption of various plasma proteins, resulting in a decreased uptake of NMs by the MPS. Of note, the shielding effect of PEGylation is governed by the surface density of the coated PEG [58] and the length of the PEG chains [97]. In general, proper density PEG coatings in the form of brush- or mushroom-like structure is crucial in protecting the NMs from opsonization [98].

Apart from PEG, a number of materials such as surfactants, polymers, proteins, or even plasma membranes, have been utilized as coating materials. Some materials can provide special functions. For example, surface coating with the surfactants, such as Tween-80 and Pluronic, is helpful to promote the NMs to cross

the blood–brain barrier [99]. RBCs have a long half-life [100], and surface coating with RBC membranes will increase the circulation time of the NMs due to the biomimetic effect [101]. Serum albumin also offers a promising material for surface modification. It has been reported that human serum albumin was used to modify the hydrophobic PLGA nanoparticles, thus yielding the hydrophilic, biocompatible surface [102].

1.6 Mathematic Simulation of NM-Mediated Cancer Drug Delivery

1.6.1 Progress: From Experiment to Simulation

The pharmacological effects correlate with the local concentration of drugs delivered by the NMs [103]. Researchers have worked on how to predict the tumor concentration of NMs (PK) and the treatment effects (PD) and establish a reliable theoretical model depicting the dynamic processes. However, the difficulties lie in the vast diversity of the NMs in the compositions and physicochemical properties, as well as the highly variable drug release behaviors in the body. Extra parameters and variations will make the simulation too complicated and less precise.

1.6.2 Compartment Models for PK Assessment of NMs

Simulations have been widely applied in drug development and safety assessment by describing the absorption, distribution, metabolism, and excretion (ADME) of small molecular drugs by using the compartment models [104]. Tissues/organs are classified into different theoretical compartments, and the drug distribution in each compartment is treated as in an equilibrium state, with homogeneous drug concentration. When the blood carries drugs with indiscriminate distribution into all the organs, the whole body can be viewed as a single compartment. Meanwhile, the drugs undergo first-order elimination. Taken together, mass balance equation for one compartment model after a single intravenously administration can be expressed as follows:

$$\frac{\mathrm{d}A_c}{\mathrm{d}t} = -k_{10}A_c,$$

where A_c and k_{10} represent drug amount in the single compartment and the first-order clearance rate constant, respectively. In general, the single-compartment model is one of the most simplified simulations based on the assumption that all the organs/tissues are homogeneous in blood flow, drug partition coefficient, as well as elimination rate. However, in most cases, great flow diversity exists among different organs/tissues. Under this circumstance, the organs with slower blood flow are categorized as peripheral compartment, and drug transport occurs

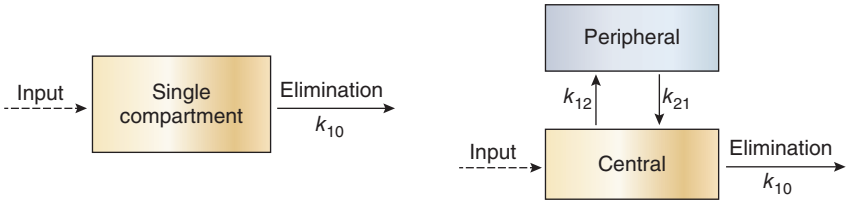

Figure 1.7 Schematic illustrations of one- and two-compartment models.

between multicompartments. Of note, drugs are supposed to be eliminated by the central compartment, because the main metabolic organs (e.g., liver and kidney) are characterized with abundant blood supply. The mass transfer balance equations for the two-compartment model are as expressed as follows:

For the central compartment:

$$\frac{dA_c}{dt} = k_{21}A_p - (k_{12} + k_{10})A_c.$$

For the peripheral compartment:

$$\frac{dA_p}{dt} = k_{12}A_c - k_{21}A_p,$$

where A_c and A_p represent the amount of drug in the central and peripheral compartments; k_{10}, the elimination rate constant, and k_{12} and k_{21} the drug transfer rate constants between the two compartments (Figure 1.7).

The conventional compartment model is a simulation of kinetic blood drug concentrations for the prediction of pharmacodynamic outcomes. The accumulation of small molecular drugs in the target organs often correlates with the blood drug concentration. However, it is different for application of the compartment models in simulating the PK behavior of NMs. As discussed above, the drug-loaded NMs vary in physicochemical properties resulting in vast diversity in biodistribution, degradation, and the drug release behavior. Consequently, the drug-loaded NMs display totally different PK profiles from those of the free drugs, providing extra challenges to build a model to predict drug concentration changes in the target sites by using the blood PK parameters. The drugs accumulate in the target sites via two pathways. First, the drug-loaded NMs distribute into the target tissues, and subsequently drugs are released therein; second, the prematurely released drugs in circulation diffuse into the target tissues. Because the encapsulated and released drugs make different contributions to the deposition in the target sites, they should be considered separately. A total drug concentration in blood is not sensitive enough to reflect actual condition. Sometimes, it may even provide misleading information, because there could be a very weak connection between drug concentrations in the blood and target tissues. In order to address this issue, additional parameters are needed to modify the model better fit for the changes.

Harashima et al. developed a simulating model for investigating the *in vivo* PK/PD of liposomal DOX in tumor tissue (Figure 1.8) [105]. The elimination

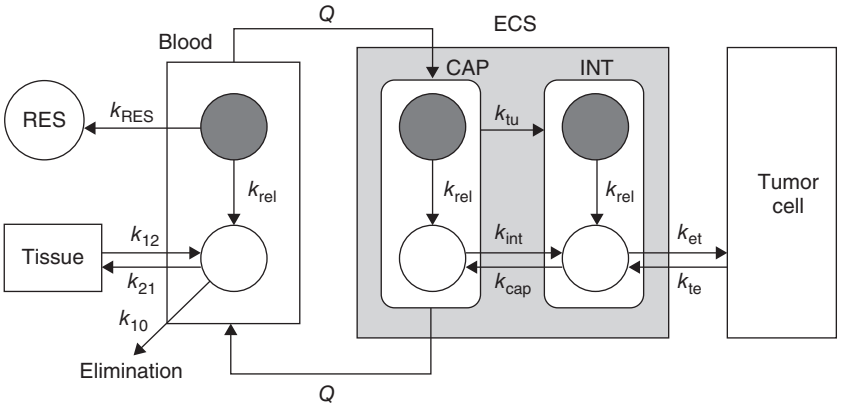

Figure 1.8 Pharmacokinetic model for free and liposomal DOX [105]. Open and closed circles represent free and liposomal DOX, respectively. Liposomal DOX in CAP was transported into INT unidirectionally (k_{tu}). Liposomal DOX was taken up by RES (k_{res}) and efflux of DOX was neglected. Rapid equilibrium was assumed between CAP and INT for free DOX and C_{ecs} was defined for free DOX in the extracellular compartment (ECS). Distribution of free DOX to tumor cells was described using k_{et} and k_{te}. The parameters k_{12}, k_{21}, and k_{10} represent the micro-pharmacokinetic constants for free DOX.

of liposomal DOX was fitted with a single-compartment model, which was characterized as liposome entrapment by the RES system without DOX release. Tumor tissue was divided into three compartments: capillary (CAP), interstitial space (INT), and tumor cells. Liposomal DOX was assumed to be in a first-order release in the blood flow (Q). The pharmacodynamics of the administrated liposomal DOX depends on the free-drug concentration in the interstitial fluid. Meanwhile, for free drugs released from liposomes, a two-compartment model was applied. The free drug undergoes a first-order elimination. A schematic illustration of the compartment model is shown in Figure 1.8.

Mass balance equations for both liposomal and free drugs are depicted as follows:

Mass balance for liposomal DOX

In blood:

$$\frac{dC_{b\,lipo} \cdot V_{b\,lipo}}{dt} = Q \cdot C_{cap\,lipo} - Q \cdot C_{b\,lipo} - (k_{RES} + k_{rel}) V_{c\,lipo} C_{b\,lipo}.$$

In RES:

$$\frac{dX_{RES}}{dt} = k_{RES} \cdot V_{c\,lipo} \cdot C_{b\,lipo}.$$

Mass balance for free drugs

In blood:

$$\frac{dC_b \cdot V_c}{dt} = k_{rel} \cdot V_{c\,lipo} \cdot C_{b\,lipo} - k_{12} \cdot V_c \cdot C_b + k_{21} \cdot X + Q \cdot C_{ecs} - Q \cdot C_b$$

In tissue:

$$\frac{dX}{dt} = k_{12} \cdot V_c \cdot C_b - k_{21} \cdot X$$

In extracellular compartment (ECS):

$$\frac{dC_{ecs} \cdot V_{ecs}}{dt} = Q \cdot C_b + k_{te} \cdot V_{tu} \cdot C_{tu} - Q \cdot C_{ecs} - k_{et} \cdot V_{ecs} \cdot C_{ecs} + k_{rel}(V_{cap} \cdot C_{cap\,lipo} + V_{int} \cdot C_{int\,lipo})$$

In tumor cell:

$$\frac{dC_{tu} \cdot V_{tu}}{dt} = k_{et} \cdot V_{ecs} \cdot C_{ecs} - k_{te} \cdot V_{tu} \cdot C_{tu}.$$

By using this model, the drug release rate and nonspecific uptake of liposomes by the RES systems could be assessed by k_{rel} and k_{res} values (Figure 1.9). The tumor Dox retention generally benefits from decreased RES uptake and a relatively faster drug release.

By taking advantage of this model, PK/PD profiles of the long-circulating liposomal DOX were simulated in a peritoneal leukemia mouse model. It was found that AUC of free DOX in interstitial space could be optimized by adjusting k_{el} value at 0.06 h^{-1} (Figure 1.9). The results were further confirmed by the PD simulation, of which k_{rel} set as 0.06 h^{-1} displayed the most proficient antitumor effect (Figures 1.10 and 1.11) [106].

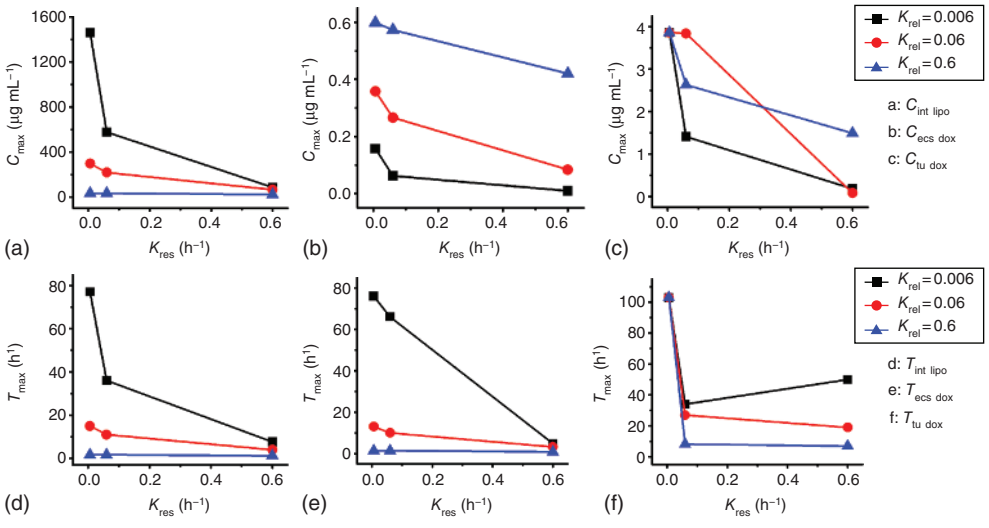

Figure 1.9 Changes of C_{max} and T_{max} in different compartments with different K_{rel} and K_{res}. The parameters $C_{int\ lipo}$, $C_{ecs\ dox}$, and $C_{tu\ dox}$ denote liposomal dox in the interstitial space, free dox in the ECS, and free dox in the tumor site, respectively; $T_{int\ lipo}$, $T_{ecs\ dox}$, and $T_{tu\ dox}$, the time at which C_{max} was reached. (Reproduced from Table 2, with permissions from Elsevier, Copyright 1999.)

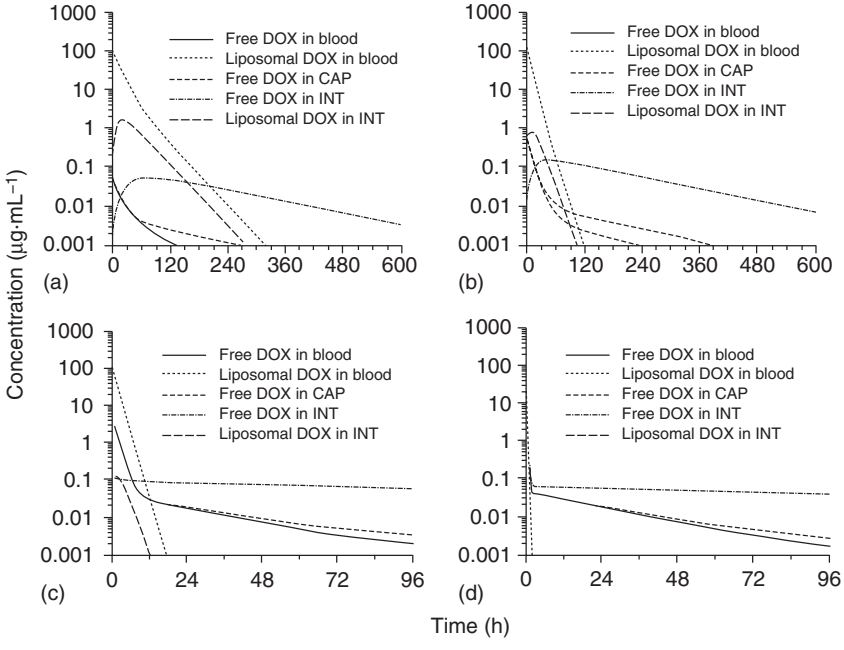

Figure 1.10 Simulations of the time courses of free and liposomal DOX in mice bearing P388 tumor in the peritoneal cavity [106]. With the other fixed parameters, while k_{rel} value was adjusted at: (a) $k_{rel} = 0.006$ (h^{-1}), (b) $k_{rel} = 0.06$ (h^{-1}), (c) $k_{rel} = 0.6$ (h^{-1}), and (d) $k_{rel} = 6$ (h^{-1}). (Reprinted with permissions from Elsevier, Copyright 1999.)

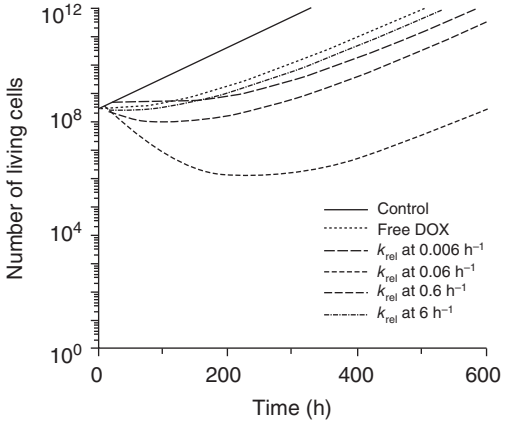

Figure 1.11 Effect of k_{rel} on the antitumor effect of liposomal DOX [106]. (Reprinted with permissions from Elsevier, Copyright 1999.)

The model is useful, especially in predicting how drugs release and the nonspecific distribution affects the delivery efficiency of the encapsulated drugs. However, this model does not take other important factors into account, such as physicochemical characters of the NMs (size, shape, zeta potential, etc.), NM-mediated tumor retention, site-specific drug release/drug delivery, and the physiological differences among organs. These factors often play important roles in NMs' ADME. Therefore, specific models should be developed for different cases in the PK/PD assessment of the drug-loaded NMs.

1.6.3
Physiologically Based Compartment Models

The development of physiologically based compartment models has provided a solid basis for the establishment of physiologically based PK (PBPK) models for NMs [107, 108]. In this method, each organ or tissue of the body with anatomically distinct structure is defined as an independent compartment. These compartments are connected with blood flow, through which the NMs enter the compartment in a perfusion- or membrane-limited pattern. Therefore, the model can be subsequently divided into different types (Figure 1.12). For the perfusion-limited model, NMs are assumed to be able to diffuse into the compartment rapidly, and the transportation is mainly governed by the local blood supply. The mass transfer balance for a certain tissue is described as follows (annotations are listed in Figure 1.12):

$$\frac{dC_T}{dt} = \frac{Q_T}{V_T} \cdot C_{ART} - \frac{Q_T}{V_T \cdot R_T} \cdot C_{VEN} - CL_T \cdot C_T.$$

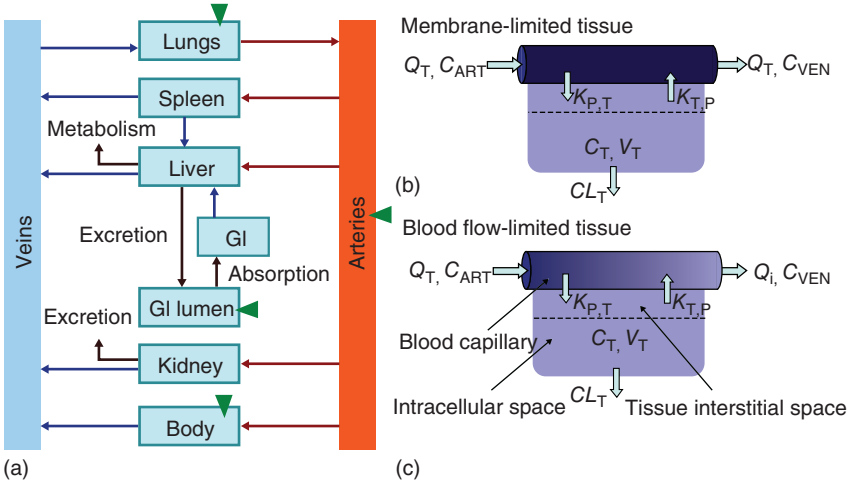

Figure 1.12 (a) A typical blood flow-limited physiologically based pharmacokinetic model structure; (b) a membrane-limited tissue; and (c) a blood flow-limited tissue [108]. (Reprinted with permissions from American Chemical Society, Copyright 2010.)

Table 1.1 Drug transport process equtions [109].

Specified process	Equations
Capillary blood flow	Navier–Stokes equation: $\rho\partial_t u_v - \mu\nabla^2 u_v + \rho(u_v \cdot \nabla)u_v + \nabla P_v = 0$
Tumor interstitial blood flow	Darcy's law: $u_i - V \cdot [KP_i] = 0$
Transmural blood flow	Starling's law: $J_v = L_p(P_v - P_i) - \sigma_d(\pi_v - \pi_i)$
Diffusion drug transport	Diffusion convection reaction equation: $\partial_t c + \nabla \cdot (-D\nabla c + uc) - R = 0$
Transmural drug transport	Kedem–Katchalsky equation: $J_F = P(c_v - c_i) + (1 - \sigma_f)J_v\overline{c}$

For the membrane-limited model, the rate-limiting step for transportation is the process of membrane penetration, and the mass balance equation is described as follows:

$$\frac{dC_T}{dt} = K_{P,T} \cdot C_{ART} - \frac{K_{T,P}}{R_T} \cdot C_T - CL_T \cdot C_T.$$

1.6.3.1 Protocols of Building a PBPK Model for NMs

Li and coworkers proposed a three-step protocol for building PBPK models for assessing the PK profile of NMs [108]. First, specific analysis of each component in the model, including the description of characteristics of the physiological compartments and NMs. Second, development of equations to describe the process of NMs/body interactions. Some equations reflecting the transport process have been summarized in Table 1.1. Generally, mass transfer balance equations are used to describe transportation of the NMs and drug release. Third, calculation of the PBPK parameters. The experimental data are input into the established equations for calculating the model parameters. The robustness of the model could also be verified by comparing the simulated data with the measured values. An optimized model should be able to predict the ADME of NMs with minimum deviation.

1.6.3.2 Examples

Size is an important factor affecting the NMs' *in vivo* distribution (e.g., the blood circulation and transmembrane processes). Bachler and coworkers developed a PBPK model to assess the biodistribution of TiO_2 nanoparticles based on their ability to cross the capillary and to be phagocytosed in the MPS [110]. The effects of the fenestrated vasculatures on capture of NMs could be divided into five groups based on the permeation of epithelial wall (Table 1.2).

In the case of excretion, high permeation of the biologically stable nano-TiO_2 into the liver resulted in more pronounced biliary excretion than the urinary pathway. The biliary/urinary ratio of excretion was estimated to be 70 : 1. The ADME processes are separately described later, and the mass balance equations can be expressed as follows:

Absorption

$$m_{absorption} = \text{nano-T}_i\text{O}_2\text{exposure} \cdot f^c_{absorption}.$$

Table 1.2 Category and feature of capillary wall from different organs [110].

Category	Features	Organs
CT1	Nonsinusoidal, nonfenestrated capillary wall	Brain, heart, lung
CT2	Nonsinusoidal, fenestrated capillary	Intestines, kidneys, stomach
CT3	Sinusoidal capillary with pores > 15 nm	Liver, spleen
CT4	Myeloid bone marrow sinusoidal capillary	Bone
CT5	Other compartment that cannot be assigned to a CT group	Hair, fat

CT, capillary wall type.

Distribution:

In blood:

$$\frac{dA_{blood}}{dt} = m_{absorption} + \sum_{organs^d} (k_{trans\text{-}organ\text{-}blood} \cdot A_{organ}) - \sum_{organs^a} (k_{trans\text{-}blood\text{-}organ} \cdot A_{blood}).$$

In organ compartment:

$$\frac{dA_{organ}}{dt} = k_{trans\text{-}blood\text{-}organ} \cdot A_{blood} - k_{trans\text{-}organ\text{-}blood} \cdot A_{organ} - k_{deposition} \cdot A_{organ},$$

where the transportation coefficient from blood to the organs was defined as:

$$k_{trans\text{-}blood\text{-}organ} = b_{trans\text{-}constant\text{-}organ} \cdot \frac{Q_{organ\text{-}blood}}{V_{blood}}$$

Organ deposition:

$$\frac{dA_{deposition}}{dt} = k_{depositon} \cdot A_{organ} - k_{clearance} \cdot A_{organ}$$

Excretion:

Biliary excretion:

$$\frac{dA_{bile\,el}}{dt} = k_{trans\text{-}blood\text{-}organ} \cdot A_{blood} + \sum_{organs^a} (k_{clearance} \cdot A_{deposition}).$$

Urinary excretion:

$$\frac{dA_{urinary\,el}}{dt} = k_{trans\text{-}blood\text{-}organ} \cdot A_{blood}.$$

It was found that in a size range of 15–150 nm, the size of nano-TiO_2 had a minor impact on the biodistribution. Furthermore, with high-dose exposure, the administrated nanoparticles tended to agglomerate and be mainly captured by the macrophages in MPS.

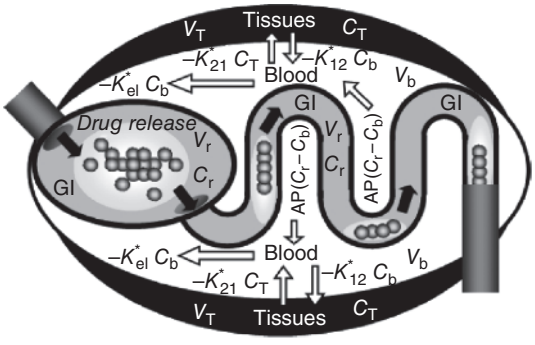

Figure 1.13 Schematic representation of drug RADME process in a polymer formulation [111]. (Reprinted with permissions from American Chemical Society, Copyright 2010.)

The modeling of drug release from NMs with mathematical methods has been extensively applied. Combination of this with the *in vivo* ADME models, however, has been rarely explored. In some cases of oral administration, the encapsulated drugs are released from NMs in GI environments. The growing complication is caused by complex process in GI tract, such as matrix swelling and erosion, drug dissolution, diffusion, and GI metabolism, giving additional variables (release behavior of drugs) to the ADME, thus termed "RADME." Grassi and coworkers presented a mathematical model for simulating the RADME process of the vinpocetine-encapsulated particles for oral administration [111]. GI tract is treated as a homogeneous compartment where drug solubility and permeability are presumed to be constant. Therefore, the GI environment is set as the central compartment, while blood and tissues are set as two "external" compartments (Figure 1.13).

The mass balance is presented by dividing the given dose of drugs (M_0) into six subgroups, including the drugs in the GI tract (V_rC_r), NMs (X), circulating system (V_bC_b), organs/tissues (V_TC_T), form of recrystallized drugs released from NMs (M_c), and excreted (M_e):

$$M_0 = V_rC_r + \sum_{j=1}^{N_c} N_{pj} \int_0^{R_{pj}} \left[C_j(R_j) + C_{dj}^{am}(R_j) + C_{dj}^{nc}(R_j) + C_{dj}^{mc}(R_j)\right] 4\pi R_j^2 dR_j + V_bC_b + V_TC_T + M_c + M_e$$

$$M_e = \int_0^t K_{el} V_b C_b dt,$$

where V_r and N_{pj} represent the volume of release medium and the number of particles belonging to the "j" class, respectively.

Drug release in the GI is treated to be equivalent to the *in vitro* release behavior, which is determined by characteristics of the drug-loaded polymer particles (but with polymer erosion being ignored), as well as concentration gradient in and outside the polymer particles. Thereby, drug release from NMs can be described as follows:

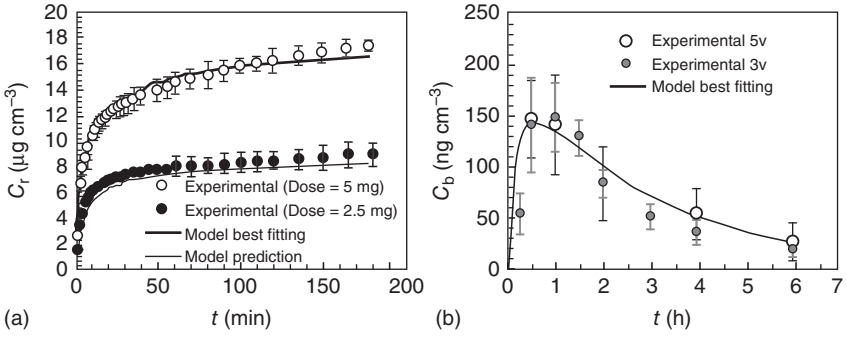

Figure 1.14 Comparison of simulated vinpocetine concentration with experimental data both *in vitro* (a, showing C_r–time profile in GI) and *in vivo* (b, showing C_b–time profile in blood). In both sets, solid lines refer to the simulated data, while open or filled circles represent experimental data from different tests [111]. (Reprinted with permissions from American Chemical Society, Copyright 2010.)

$$\frac{\partial C_{pj}}{\partial t} = \frac{1}{R_j^2}\frac{\partial}{\partial R_j}\left(D\frac{\partial C_j}{\partial R_j}R_j^2\right) - \left(\frac{\partial C_{dj}^{am}}{\partial t} + \frac{\partial C_{dj}^{nc}}{\partial t} + \frac{\partial C_{dj}^{mc}}{\partial t}\right)$$
$$j = 1, 2, 3, \ldots N_c,$$

where C_j is the concentration of the dissolved drug at radius R_j inside the particles of the jth class;C_{dj}^{am}, C_{dj}^{nc}, and C_{dj}^{mc} are, respectively, the concentrations of the nondissolved drug in the amorphous, nanocrystalline, and macrocrystalline states at radius R_j inside the particles of the jth class; and D is the drug diffusion coefficient (depending on $C_{pj}(R_j)$).

Blood concentration C_b changes as a result of the combined contribution of drug influx from GI tract fluid, distribution into (or redistribution from) the organs, and elimination. Thus the differential equation is defined as

$$V_b\frac{dC_b}{dt} = AP(C_r - C_b) - K_{el}^*C_b - K_{12}^*C_b + K_{21}^*C_T.$$

The simulated data were found to fit well with experimental results (Figure 1.14), providing a good prediction of ADME processes.

1.6.4 Brief Summary

Despite the efforts that have been made in simulating the PK of NMs, the developed models are biased, because the algorithms are primarily built to simulate a few parts of the whole dynamic process, with other parts being simplified to reduce complexity of the simulation. For example, the model developed by Bachler and coworkers provided a good interpretation of the influence of the fenestrated capillaries on capture of the hard-matter nanoparticles, but it may not be sensitive in assessing the PK profiles of biodegradable NMs. As for the work of Grassi and coworkers, since the simulation is based on the model that drugs are released

from NMs before absorption by the GI tract, the model is not applicable when the drugs are loaded onto NMs via specifically designed covalent bonds. The drawback of the biased simulation is that the model only responds to changes of the parameters that are built in the functions.

However, the PK of drug-loaded NMs is a very complicated process with each component varying distinctly depending on different design. In order to make the model feasible to a wide application, additional factors concerning features of NMs (opsonization, receptor-mediated binding and internalization, site-specific release, etc.) and the body (receptor density, blood perfusion, enzyme activity, physiological volume of the organs, etc.) should be taken into account. On the contrary, the incorporation of additional parameters to the functions will dramatically increase the complexity of the model. As a solution, the transportation parameters that derive from a series of interrelated parameters are introduced. For example, the multiple properties of NMs, such as size, zeta potential, and PEGylation, could be transformed into an individual parameter by a certain function (i.e., linear multivariate regression) [112].

Furthermore, establishment of a PBPK model for NMs is an interdisciplinary work that includes characterization of the physicochemical properties of NMs, specification of physiological systems, and mathematical simulation. Therefore, it requires collaboration of professionals from different fields such as physiology, physical chemistry, nanotechnology, mathematics, and computer science. Importantly, the robustness of the model is needed to be improved, which requires a great amount of high-quality training data [113].

1.7 Experimental PK Data of the Applied NMs

Owing to the development of nanotechnology, a variety of NMs are currently available for market and clinical trials in drug delivery. Here, we summarize the PK data of a number of NM-loaded drugs including paclitaxel [114–116], doxorubicin [117–121], curcumin [122–124], and large molecules such as siRNA [125] and insulin (Tables 1.3 and 1.4) [126, 127, 133]. By comparing the PK behaviors of drugs encapsulated by different NMs, it would be helpful to get a better understanding on how the physiochemical changes of NMs affect the ADME:

1. Size. In a study using PAMAM dendrimer for calcitonin delivery, it was found that the pharmacological effect was enhanced when large PAMAM was used: the pharmacological availability (PA) was increased from 22.0% to 27.6% in a comparison between the G0 polymer and G3 dendrimer [141]. However, in the case of orally administered drugs, small NMs may be superior to the large ones in transporting across the intestinal membrane. Similarly, PEGylation that help prevent NMs from aggregation under physiological conditions was demonstrated to be effective to increase the oral bioavailability of the encapsulated drugs [121].

Table 1.3 PK data of drug-loaded natural NMs.

NM		Description	PK data	References
Polymers	Chitosan NP	Chitosan/glyceryl-monooleate + paclitaxel	i.v., mice, AUC, 1.08 μg mL d^{-1} (1.46-fold); Vd, 165.8 mL; MRT, 20.49 d; tumor AUC, 132.9 ± 20.5 (20.4-fold); Kp ratio for tissue/plasma was 11.6 ± 2.9 (96.9-fold)	[114]
	Chitosan NP	*N*-Octyl-*O*-sulfate chitosan micelle + paclitaxel; 200.8 nm, −28.8 mV	i.v., rats, 7 mg kg^{-1}, AUC, 3009.9 ± 877.1 μg L^{-1} h; CL, 2.49 ± 0.98 L h^{-1} kg^{-1}; MRT, 2.03 ± 0.25 h; Vd, 7.06 ± 2.89 L kg^{-1}	[115]
	Chitosan NP	Chitosan/poly(g-glutamic acid) + aspart-insulin; 245.4 nm, 26.8 mV	Rats, p.o., 30.0 IU kg^{-1}, AUC, 140.4 ± 24.3 μIU mL^{-1} h; C_{max}, 38.5 ± 11.4 μIU mL^{-1}; BA_r, 15.7 ± 1.2%	[126]
	Chitosan NP	Chitosan/poly(g-glutamic acid) + insulin; 232.9 nm, 26.3 mV	p.o., 30 IU kg^{-1}, rats, AUC, 235.8 ± μIU mL^{-1} h; C_{max}, 49.9 ± 2.4 μIU mL^{-1}; T_{max}, 5 h	[127]
	Histidine–lysine	Histidine–lysine + siRNA	i.v., mice, AUC_{0-2h}, 98.0 ± 58.6 μg mL^{-1} min; MRT, 129.5 min; CL, 16.62 mL kg^{-1} min^{-1}; BA 0.78-fold	[125]
	Histidine–lysine	RGD-PEG-histidine–lysine + siRNA	i.v., mice, AUC_{0-2h}, 385.0 ± 58.6 μg mL^{-1} min; MRT, 374.7 min; CL, 1.57 mL kg^{-1} min^{-1}; BA 3.05-fold	[125]
	Dendrimer	PEGylated dendrimer loaded dox via acid-labile linker; G5	i.v., rats, AUC, 341 ± 39 μg mL^{-1} h; Vd, 27.5 ± 9.4 mL; CL, 0.97 ± 0.20 mL h^{-1}; BA increased 811.9-fold	[117]
Liposome	Liposome	CD19 antibody-modified (HSPC + cholesterol) + doxorubicin; 100 ± 10 nm	i.v., mice. For dox: AUC, 60.0 mg kg^{-1} h; $t_{1/2(CL)}$, 19.2 h; $t_{1/2(release)}$, 315.0 h; for phospholipid: AUC, 318.4 mg kg^{-1} h; $t_{1/2(CL)}$, 20.6 h	[118]
	Liposome	CD19 antibody-modified (DPPC + cholesterol) + doxorubicin; 100 ± 10 nm	i.v., mice. For dox: AUC, 56.5 mg kg^{-1} h; $t_{1/2(CL)}$, 16.9 h; $t_{1/2(release)}$, 125.0 h; for phospholipid: AUC, 229.0 mg kg^{-1} h; $t_{1/2(CL)}$, 19.1 h	[118]
	Liposome	CD19 antibody-modified (PMPC + cholesterol) + doxorubicin; 100 ± 10 nm	i.v., mice. For dox: AUC, 40.4 mg kg^{-1} h; $t_{1/2(CL)}$, 14.4 h; $t_{1/2(release)}$, 65.0 h; for phospholipid: AUC, 239.6 mg kg^{-1} h; $t_{1/2(CL)}$, 17.6 h	[118]
	Liposome	CD19 antibody-modified (POPC + cholesterol) + doxorubicin; 100 ± 10 nm	i.v., mice. For dox: AUC, 48.8 mg kg^{-1} h; $t_{1/2(CL)}$, 13.1 h; $t_{1/2(release)}$, 40.5 h; for phospholipid: AUC, 233 mg kg^{-1} h; $t_{1/2(CL)}$, 17.7 h	[118]

	Liposome	CD19 antibody-modified (DOPC + cholesterol) + doxorubicin; 100 ± 10 nm	i.v., mice. For dox: AUC, 19.5 mg kg^{-1} h; $t_{1/2(CL)}$, 7.6 h $t_{1/2(release)}$, 1.9 h; for phospholipid: AUC, 182.0 mg kg^{-1} h; $t_{1/2(CL)}$, 15.7 h	[118]
	Liposome	Stealth liposome + doxorubicin; 100 ± 20 nm	i.v., mice, AUC, 1417.6 μmol mL^{-1} h; CL, 0.08 mL h^{-1}; Vd, 1.7 mL; MRT, 19.9 h	[128]
	Liposome	Fv fragment of CD 19 antibody-modified stealth liposome + doxorubicin; 100 ± 20 nm	i.v., mice, AUC, 997.7 μmol mL^{-1} h; CL,0.12 mL h^{-1}; Vd, 1.7 mL; MRT, 14.2 h	[128]
	Liposome	Fab' fragment of CD 19 antibody-modified stealth liposome + doxorubicin; 100 ± 20 nm	i.v., mice, AUC, 1291.2 μmol mL^{-1} h; CL, 0.10 mL h^{-1}; Vd, 1.8 mL; MRT, 18.1 h	[128]
	Liposome	Whole CD19 antibody-modified stealth liposome + doxorubicin; 100 ± 20 nm	i.v., mice, AUC, 292.6 μmol mL^{-1} h; CL, 0.41 mL h^{-1}; Vd, 2.3 mL; MRT, 5.6 h	[128]
	Liposome	PEGylated liposome + dox	i.v., rats. AUC, 1786 ± 367 μg mL^{-1} h; Vd, 6.6 ± 1.5 mL; CL, 0.19 ± 0.02 mL h^{-1}; BA increased 4252.4-fold	[117]
	Liposome	PEG-liposome + dox; 100.7 nm, −20.1 mV	AUC, 2183 ± 460 μg mL h; MRT, 26.96 ± 4.01 h; $t_{1/2\beta}$, 25.32 ± 4.89 h; CL 0.69 ± 0.07 mL h^{-1}; BA increased 8.3-fold	[119]
	Liposome	RGD-PEG-liposome + dox; 114.1 nm, −24.9 mV	AUC, 1679 ± 189 μg mL h; MRT, 21.88 ± 0.97 h; $t_{1/2\beta}$, 24.10 ± 2.42 h; CL 1.10 ± 0.05 mL h^{-1}; BA increased 6.4-fold	[119]
	Liposome	PEGylated liposome + dox	i.v., rats 6 mg kg^{-1}, Mice, AUC, 2257.5 μg mL^{-1} h; T_{max}, 3 h; C_{max}, 2.18 μg mL^{-1}; BA increased 1461-fold	[120]
SLNs	Lipid NP	SLN + dox; 280.2 nm, but may increased to 462.3 nm after incubated with intestinal fluids	p.o., rats, C_{max}, 1.90 μg mL^{-1}; T_{max}, 1.5 h, AUC_{0-t}, 17.79 μg mL^{-1} h; MRT, 22.87 h; Ke, 0.2 h^{-1}; BA 377.7%	[121]
	Lipid NP	PEGylated SLN + dox; 150.2 nm, and remains stable in intestinal fluids	p.o., rats, C_{max}, 2.26 μg mL^{-1}; T_{max}, 0.5, 4 h, AUC_{0-t}, 35.4 μg mL^{-1} h; MRT, 33.03 h; Ke, 0.07 h^{-1}; BA 751.6%	[121]
	Lipid NP	CTAB-coated lipid nanocapsule + fondaparinux; 58.2 nm, 42.9 mV	p.o., rats 5mg kg^{-1}, rats, AUC, 336.5 ± 187.3 μg mL^{-1} min; MRT, 177.1 ± 82.6 min; CL, 450.7 ± 7.1 mL min^{-1}; C_{max}, 0.98 ± 0.33 mL^{-1}; BA increased 6.9-fold	[129]

(*continued overleaf*)

Table 1.3 (*continued*)

NM	Description	PK data	References
Lipid NP	Stearylamine-coated lipid nanocapsule + fondaparinux; 48.1 nm, 4.0 mV	p.o., 5mg kg^{-1}, rats, AUC, 730.9 ± 214.9 μg mL^{-1} min; MRT, 338.4 ± 69.4 min; CL, 485.9 ± 13.8 mL min^{-1}; C_{max}, 1.31 ± 0.37 mL^{-1}; BA increased 15.0-fold	[129]
Lipid NP	Tetradecanoic acid SLN + enrofloxacin; 116.7 nm, −29.0 mV	i.m., mice, AUC, 33.7 ± 2.5 mg L^{-1} h; C_{max}, 1.7 ± 0.1 μg mL^{-1}; MRT, 180.4 ± 36.2 h; CL, 0.02 ± 0.002 mL^{-1} h^{-1}; BA increased 7.2-fold	[130]
Lipid NP	Palmitic acid SLN + enrofloxacin; 111.0 nm, −31.6 mV	i.m., mice, AUC, 17.7 ± 2.7 mg L^{-1} h; C_{max}, 1.9 ± 0.1 μg mL^{-1}; MRT, 46.3 ± 10.1 h; CL, 0.058 ± 0.007 mL^{-1} h^{-1}; BA increased 3.7-fold	[130]
Lipid NP	Stearic acid SLN + enrofloxacin; 217.3 nm, −40.0 mV	i.m., mice, AUC, 11.9 ± 0.8 mg L^{-1} h; C_{max}, 2.0 ± 0.2 μg mL^{-1}; MRT, 19.1 ± 2.9 h; CL, 0.079 + 0.013 mL^{-1} h^{-1}; BA increased 2.4-fold	[130]
Lipid NP	(Soylecithin, P188, trimyristin) + clozapine; 233.3 nm, 0.2 mV	i.v., 10 mg kg^{-1}, rats, AUC, 9.67 ± 1.86 μg mL^{-1} h; CL, 1.07 ± 0.2 L h^{-1} kg^{-1}; MRT, 8.92 ± 1.28 h; BA increased 1.51-fold	[131]
Lipid NP	(Soylecithin, P188, stearylamine, trimyristin) + clozapine; 150.2 nm, 33.2 mV	i.v., 10 mg kg^{-1}, rats, AUC, 13.72 ± 1.7 μg mL^{-1} h; CL, 0.74 ± 0.1 L h^{-1} kg^{-1}; MRT, 9.52 ± 1.85 h; BA increased 2.15-fold	[131]
Lipid NP	(Soylecithin, P188, stearylamine, tripalmitin) + clozapine; 163.3 nm, 23.2 mV	i.v., 10 mg kg^{-1}, rats, AUC, 10.55 ± 1.26 μg mL^{-1} h; CL, 0.96 ± 0.11 L h^{-1} kg^{-1}; MRT, 8.97 ± 1.62 h; BA increased 1.65-fold	[131]
Lipid NP	(Soylecithin, P188, stearylamine, tristearin) + clozapine; 96.7 nm, 21.3 mV	i.v., 10 mg kg^{-1}, rats, AUC, 18.58 ± 1.13 μg mL^{-1} h; CL, 0.54 ± 0.02 L h^{-1} kg^{-1}; MRT, 10.72 ± 1.36 h; BA increased 2.91-fold	[131]
Lipid NP	SLN (Precirol ATO-5, Labrafil M 1944CS) + tripterine; 102.4 nm, −26.2 mV	p.o., dogs, AUC, 1792.0 ± 57.1 μg L^{-1} h; C_{max}, 305.0 ± 35.4 μg L^{-1}; $t_{1/2}$, 3.85 ± 0.94 h; MRT, 4.37 ± 0.33 h; BA increased 2.86-fold	[132]
Lipid NP	CPP-modified SLN (Precirol ATO-5, Labrafil M 1945CS) + tripterine; 126.7 nm, 28.7 mV	p.o., dogs, AUC, 2568.0 ± 343.4 μg L^{-1} h; C_{max}, 483.0 ± 15.4 μg L^{-1}; $t_{1/2}$, 3.09 ± 0.54 h; MRT, 4.08 ± 0.37 h; BA increased 4.10-fold	[132]

Table 1.4 PK data of drug-loaded synthetic NMs.

NM		Description	PK data	References
NPs	PLGA NP	PEGylated PLGA + insulin; 189.6 nm, −34.0 mV	p.o., 10 IU kg^{-1}, rats. 5672 ± 4006 μIU mL^{-1} min	[133]
	PLGA NP	L-R8-modified PEGylated PLGA + insulin; 196.8 nm, 14.7 mV	p.o., 10 IU kg^{-1}, rats. 13 570 ± 8059 μIU mL^{-1} min	[133]
	PLGA NP	R-R8-modified PEGylated PLGA + insulin; 200.1 nm, 15.3 mV	p.o., 10 IU kg^{-1}, rats. 19 145 ± 10 876 μIU mL^{-1} min	[133]
	Polyanhydride NP	NP + paclitaxel; 177 nm, −44.2 mV	p.o., rats, AUC, 7.4 ± 0.9 μg mL^{-1} h; C_{max}, 0.2 ± 0.0 μg mL^{-1}; MRT, 31 ± 1 h; $t_{1/2}$, 27 ± 1 h	[134]
	Polyanhydride NP	PEG2k-NP + paclitaxel; 178 nm, −40.3 mV	p.o., rats, AUC, 56 ± 3 μg mL^{-1} h; C_{max}, 2.1 ± 0.1 μg mL^{-1}; MRT, 26 ± 1 h; $t_{1/2}$, 9.3 ± 0.5 h	[134]
	Polyanhydride NP	PEG6k-NP + paclitaxel; 180 nm, −39.5 mV	p.o., rats, AUC, 32 ± 2 μg mL^{-1} h; C_{max}, 1.9 ± 0.1 μg mL^{-1}; MRT, 27 ± 1 h; $t_{1/2}$, 6.2 ± 0.3 h	[134]
	Polyanhydride NP	PEG10k-NP + paclitaxel; 188 nm, −41.1 mV	p.o., rats, AUC, 13 ± 1 μg mL^{-1} h; C_{max}, 1.4 ± 0.1 μg mL^{-1}; MRT, 18 ± 1 h; $t_{1/2}$, 29 ± 2 h	[134]
	PLGA NP	PLGA NP + gentamicin; PLGA 50:50, 13.7 kDa, 1.84 ± 0.70 μm	i.v., mice, liver: AUC, 468.3 ± 58.7 μg g^{-1} d (390.3-fold); MRT, 13.7 d; spleen: AUC, 416.0 ± 168 μg g^{-1} d (462.2-fold); MRT, 45.0 d; kidney: AUC, 109.3 ± 3.3 μg g^{-1} d (7.3-fold); MRT, 1.7 d	[135]
	PLGA NP	PLGA NP + gentamicin; PLGA 75:25, 25 kDa, 2.5 ± 0.17 μm	i.v., mice, liver: AUC, 425.0 ± 55 μg g^{-1} d (354.2-fold); MRT, 13.9 d; spleen: AUC, 745.3 ± 55.7 μg g^{-1} d (828.1-fold); MRT, 60.4 d; kidney: AUC, 221.7 ± 30.7 μg g^{-1} d (14.8-fold); MRT, 1.6 d	[135]
	PLGA NP	Cylindrical shape NP + docetaxel; 200 × 200 nm ($d \times h$); −3.4 mV	i.v., mice, AUC_{0-72h}, 134 429 ng mL^{-1} h; CL, 72 mL kg^{-1} h; Vd, 257 mL kg^{-1}; BA increased 23.1-fold; for tumor: AUC_{0-24h}, 79 644 ng mL^{-1} h; C_{max}, 4413 ± 323 ng mL^{-1}; BA increased 1.3-fold	[136]

(*continued overleaf*)

Table 1.4 (*continued*)

NM		Description	PK data	References
	PLGA NP	Cylindrical shape NP + docetaxel; 80 × 320 nm ($d \times h$); −3.2 mV	i.v., mice, AUC_{0-72h}, 133 462 ng mL^{-1} h; CL, 73 mL kg^{-1} h; Vd, 474 mL kg^{-1}; BA increased 23.0-fold; for tumor: $AUC_{0-24h,}$ 95 516 ng mL^{-1} h; C_{max}, 4187 ± 23 ng mL^{-1}; BA increased 1.5-fold	[136]
	PLGA	PLGA NP + curcumin; 161.9 nm	p.o., 50 mg kg^{-1}, rats, AUC, 134.25 ± 3.45 ng mL^{-1} h; C_{max}, 11.78 ± 0.45 ng mL; T_{max}, 2 h; Ke, 0.18 ± 0.02 h^{-1}; Vd, 2073.66 ± 352.61 L kg^{-1}; CL, 365.19 ± 37.35 L kg^{-1} h^{-1}; BA increased 15.6-fold	[122]
	PLGA	PEG-PLGA + curcumin; 152.4 nm	p.o., 50 mg kg^{-1}, rats, AUC, 447.80 ± 64.03 ng mL^{-1} h; C_{max}, 29.78 ± 4.63 ng mL; T_{max}, 3 h; Ke, 0.18 ± 0.02 h^{-1}; Vd, 900.54 ± 225.77 L kg^{-1}; CL, 103.679 ± 10.90 L kg^{-1} h-2; BA increased 55.5-fold	[122]
	Polymeric NP	Polystyrene beads; 300 nm	Oral, mice, BD at day 1: brain 14.3%, heart 12.8%, kidney 28.2%, lung 3.4%, liver 41.3%, spleen 0.2%; BD at day 7: brain 13.6%, heart 10.5%, kidney 18%, lung 2.9%, liver 53%, spleen 2%	[137]
	Polymeric NP	Rhodamine NP; 374 nm, −(10 − 18) mV	Oral, mice, BD at day 1: brain 16.4%, heart 21.3%, kidney 25.9%, lung 4.2%, liver 41.3%, spleen 1.7%; BD at day 7: brain 10.1%, heart 15.7%, kidney 18.3%, lung 11.4%, liver 38.1%, spleen 6.4%	[137]
	Polymeric NP	Coumarine NP; 375 nm, −(10 − 18) mV	Oral, mice, BD at day 1: brain 10.8%, heart 9.4%, kidney 23.1%, lung 2.7%, liver 52.9%, spleen 1.1%; BD at day 7: brain 18.1%, heart 14%, kidney 27.1%, lung 4.7%, liver 33.4%, spleen 2.7%	[137]
Micelles	Copolymeric micelle	PLGA-PEG-PLGA micelle + curcumin; 26.3 nm, −0.71 mV	I.V., 10 mg kg^{-1}, Mice. AUC, 621.6 ± 24.7 μg L^{-1} h; C_{max}, 2.17 ± 0.10 μg mL^{-1}; MRT, 0.90 dd ± 0.11 h; CL, 16.11 ± 0.66 mL^{-1} h^{-1}; BA increased 1.31-fold; liver: AUC, 546.1 μg L^{-1} h (3.85-fold); spleen: AUC, 213.7 μg L^{-1} h (0.34-fold); lung: AUC, 6922.8 μg L^{-1} h (5.56-fold)	[123]

	Polymeric micelle	Polyethylene glycol poly(glutamic acid) block copolymers + cisplatin; 30 nm	i.v., rats, AUC, 1325.9 ± 77.9 mL^{-1} h (64.7-fold); CL, 3.77 ± 0.21 mL h^{-1} kg^{-1}; MRT, 10.67 ± 0.15 h; Vss, 40 ± 2.3 mL kg^{-1}	[138]
	Polymeric micelle	PCL-PEG-PEG + curcumin; 62.4 nm, −4.25 mV	i.v., rats, AUC, 2772.5 μg mL^{-1} h^{-1}; CL, 5 mL h^{-1} kg^{-1}; MRT, 30.07 h; Vss, 0.216 L kg^{-1}; BA increased 4.15-fold	[124]
	Polymeric micelle	PEG-polyaspartate micelle + paclitaxel, 85 nm	i.p., mice, AUC, 191 ± 32.1 μg mL^{-1} h; BA increased 127.3-fold, compared with cremophor EL formulation	[116]
	Polymeric micelle	PEG-poly(methacrylic acid) + cisplatin; 110 nm, −12 mV	i.v., mice, AUC, 707.03 μg mL^{-1} h; Vss, 1.69 L kg^{-1}; MRT, 12.37 h; BA increased 21.68-fold; tissue AUC: for kidney, 372 μg g^{-1} h (1.39-fold); for liver, 2291 μg g^{-1} h (9.75-fold); for spleen, 12 115 μg g^{-1} h (178.16-fold); for tumor, 170 μg g^{-1} h (3.15-fold)	[139]
Dendrimer	PAMAM	G4 PAMAM + indomethacin	i.v., 3.3 mg kg^{-1}, rats, AUC, 125.9 ± 22.3 μg mL^{-1} h; MRT, 5.72 ± 0.47 h; BA increased 1.37-fold; AUC for target organ, 396.4 ± 18.7 μg mL^{-1} h (1.91)	[140]
	PAMAM	Folic acid-modified G4 PAMAM + indomethacin; folic acid: PAMAM = 3.86	i.v., 3.3 mg kg^{-1}, rats, AUC, 127.6 ± 25.2 μg mL^{-1} h; MRT, 6.60 ± 0.01 h; BA increased 1.39-fold; AUC for target organ,579.0 ± 19.3 μg mL^{-1} h (2.79)	[140]
	PAMAM	Folic acid-modified G4 PAMAM + indomethacin; folic acid: PAMAM = 11.9	i.v., 3.3 mg kg^{-1}, rats, AUC, 121.2 ± 1.9 μg mL^{-1} h; MRT, 7.77 ± 1.70 h; BA increased 1.32-fold; AUC for target organ, 602.9 ± 22.2 μg mL^{-1} h (2.91)	[140]
	PAMAM	Folic acid-modified G4 PAMAM + indomethacin; folic acid: PAMAM = 21.4	i.v., 3.3 mg kg^{-1}, rats, AUC, 166.6 ± 0.2 μg mL^{-1} h; MRT, 7.03 ± 0.07 h; BA increased 1.81-fold; AUC for target organ, 850.7 ± 20.6 μg mL^{-1} h (4.10)	[140]
	PAMAM	PAMAM G3 + insulin; 1% PAMAM	Pulmonary absorption, rats. AUC, $27\,916.8 \pm 2140.8$ mU mL^{-1} min; BA %, 40.4 ± 3.1% (4.2-fold)	[141]
	PAMAM	PAMAM G0 + calcitonin; 1% PAMAM	Pulmonary absorption, rats. PA%, 22.0 ± 0.8% (2.3-fold)	[141]

(*continued overleaf*)

Table 1.4 (*continued*)

NM		Description	PK data	References
	PAMAM	PAMAM G1 + calcitonin; 1% PAMAM	Pulmonary absorption, rats. PA%, 23.7 ± 0.7% (2.4-fold)	[141]
	PAMAM	PAMAM G2 + calcitonin; 1% PAMAM	Pulmonary absorption, rats. PA%, 25.0 ± 2.7% (2.6-fold)	[141]
	PAMAM	PAMAM G3 + calcitonin; 1% PAMAM	Pulmonary absorption, rats. PA%, 27.6 ± 1.6% (2.8-fold)	[141]
	PAMAM	G4-PAMAM-NH2 + simvastatin; 0.1% w/v PAMAM	p.o., 5 mg kg^{-1}, rats. AUC, 19.03 ± 1.28 mL $^{-1}$ h; MRT, 5.9 ± 0.37 h; ke, 1.840; BA increased 5.60-fold	[142]
	PAMAM	G4-PAMAM-OH + simvastatin; 0.1% w/v PAMAM	p.o., 5 mg kg^{-1}, rats. AUC, 11.14 ± 1.51 mL $^{-1}$ h; MRT, 7.2 ± 0.11 h; ke, 0.114; BA increased 3.28-fold	[142]
	PAMAM	G4-PAMAM-PEG + simvastatin; 0.1% w/v PAMAM	p.o., 5 mg kg^{-1}, rats. AUC, 25.43 ± 2.16 mL $^{-1}$ h; MRT, 6.6 ± 0.18 h; ke, 0.570; BA increased 7.48-fold	[142]
	Dendritic lysine	Peg5k-dendritic lysine-cholic acid (PEG5k-CA8) + paclitaxel	i.v., mice, AUC, 21 827 ng mL^{-1} h; C_{max}, 54 730 ng mL^{-1}; CL, 687 L h^{-1} kg^{-1}; Vd, 69 758 L kg^{-1}	[143]
	Dendritic lysine	Peg5k-dendritic lysine-cholic acid (PEG5k-CA8) + daunorubicin; nontargeted dendrimer	i.v., 10 mg kg^{-1}, mice, AUC, 28 333 ± 833 μg mL^{-1} h^2; Vss, 10.45 ± 1.41 mL kg^{-1}; CL, 0.01 ± 0.00 mL min^{-1} kg^{-1}; MRT, 1648 ± 209 h; BA increased 33.92-fold	[144]
	Dendritic lysine	CLL1-Peg5k-dendritic lysine-cholic acid (PEG5k-CA8) + daunorubicin; targeted dendrimer, 14 nm	i.v., 10 mg kg^{-1}, mice, AUC, 26 667 ± 6333 μg mL^{-1} h^2; Vss, 16.10 ± 1.58 mL kg^{-1}; CL, 0.01 ± 0.001 mL min^{-1} kg^{-1}; MRT, 2682 ± 860 h; BA increased 31.9-fold	[144]
	Dendritic lysine	Peg5k-dendritic lysine-cholic acid (PEG5k-CA8) + daunorubicin; nontargeted dendrimer	i.v., 5 mg kg^{-1}, rats, AUC, 90.1 ± 13.1 μg mL^{-1} h^2; Vss, 1355.6 ± 9.0 mL kg^{-1}; CL, 0.93 ± 0.14 mL min^{-1} kg^{-1}; MRT, 24.4 ± 3.7 h; BA increased 25.0-fold	[144]
	Dendritic lysine	CLL1-Peg5k-dendritic lysine-cholic acid (PEG5k-CA8) + daunorubicin; targeted dendrimer, 14 nm	i.v., 5 mg kg^{-1}, rats, AUC, 79.2 ± 4.4 μg mL^{-1} h^2; Vss, 1743.9 ± 47.1 mL kg^{-1}; CL, 1.05 ± 0.06 mL min^{-1} kg^{-1}; MRT, 27.7 ± 2.3 h; BA increased 22.0-fold	[144]

2. Components. By adjusting the constituents, the features of NMs, such as size, zeta potential, and hydrophobicity, can be changed, thereby leading to different blood PK of the loading drugs [130, 131, 135].
3. Shape. In line with the findings that NMs with high aspect ratio were less-efficiently phagocytized by MPS, cylinder PLGA nanoparticles with low aspect ratio (200 nm × 200 nm, $d \times h$) were more readily captured by the RES organs, compared with elongated ones (80 nm × 320 nm, $d \times h$), and thus was more effective in improving the BA of encapsulated drugs [136].
4. Surface coating. PEGylation is effective in improving systemic circulation of NMs. For example, the blood clearance rate (CL) and mean resident time (MRT) of Dox [121] and curcumin [122] in the nanoformulations were greatly extended with PEGylation. Surfactant coating was also effective in adjusting the surface characteristics of NMs, and thus changed blood PK of the drugs [129].
5. Ligand modification. Generally, ligand modification promotes preferential uptake by the target organ. In order to increase the targeting efficiency for indomethacin delivery, PAMAMs modified with different amounts of folic acid were investigated. The BA of the drugs in the target organ increased when the dendrimer was coupled with more folate molecules. However, ligand modification may also cause unfavorable changes of the NMs and lead to accelerated elimination of NMs from the blood [119], or decreased blood concentration due to increased volume of apparent distribution (Vd) [144], which may account for the decreased blood BA. As a potential solution, small and active fragments may be utilized. For example, the liposomes modified with the Fab′, or Fv fragment from CD 19 antibody can lower CL and Vd, with 3.4-fold increase in blood AUC of the encapsulated dox compared with those modified with the whole antibody (1291.2 $\mu g\,mL^{-1}\,h$ vs 292.6 $\mu g\,mL^{-1}\,h$) [128].
6. CPP modification. CPP modification enhances transport efficiency of NMs, and has been applied for oral drug delivery. It was demonstrated that the oral BA of tripterine [132] and insulin [133] was increased when NM loading was modified with CPPs.

It should be mentioned that the PK profiles are also affected by many other factors such as intrinsic features of the drugs and routes of administration. All these factors contribute to diversity of the drug biofate.

1.7.1 PK Data of NMs Without Drugs

Dendrimers or metallic nanoparticles are useful tools for investigating NMs' PK parameters, because the NMs can be conveniently tailored with tunable size or modified with different ligands. For example, by using dendritic polylysines, it was found that the blood clearance rate decreased from 194 to 0.4 $mL\,h^{-1}$ when the MW increased from 6 to 68 kDa [97]. Furthermore, the incorporation of lipophilic

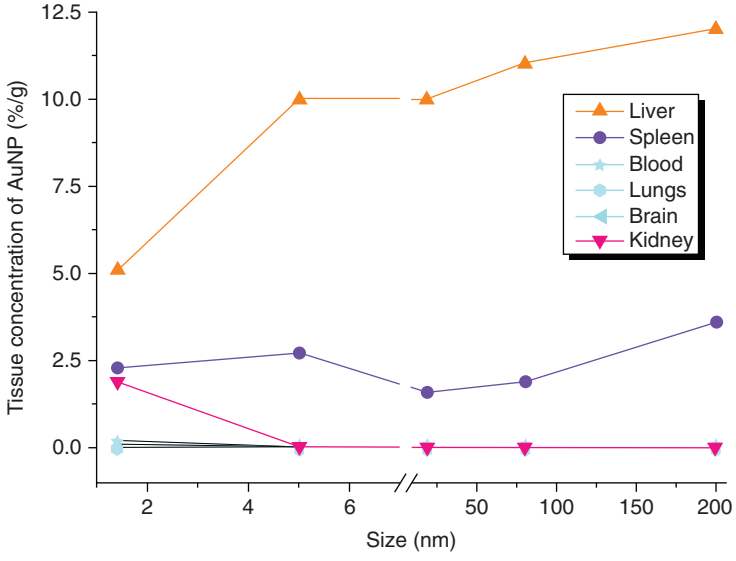

Figure 1.15 Organ content of triphenylphosphine-coated AuNP with different size.

drugs can increase the surface hydrophobicity of the dendrimer, leading to a rapid blood clearance [145]. Although the RES organs have different "appetites" on the uptake of particles, PK results of triphenylphosphine-modified gold nanoparticles of size 1.4–200 nm revealed that the liver remained the most preferential target of the injected NMs [146]. By plotting the tissue concentration against the particle size, it was further depicted that the particle retention by the liver and spleen increased together with the increase of particle size, whereas renal content decreased as the particle size was increased to 5 nm, in line with the reported "cutoff" size of renal clearance (Figure 1.15). Other factors, such as zeta potential and surface coating, could also be adjusted and lead to different PK profiles, which are summarized in Table 1.5.

1. Long-chain PEGs are more effective than their short-chains counterparts to create dense surface polymer coating [145]. Besides, the brush- and mushroom-like PEG confirmations are the most effective forms in protecting NMs from rapid clearance [98].
2. Renal clearance is a major way for elimination of ultrafine particles, but it decreases once the NMs' size surpasses the renal "cutoff." Uptake by the RES organ becomes the major clearance route for the large NMs.

1.7.2 PK Differences Between Drugs Encapsulated by Different NMs

PK analysis of different formulations for a certain drug enables the selection of the suitable NMs for efficient delivery. Table 1.6 lists the PK data of paclitaxel

Table 1.5 PK data of some NMs.

NM		Description	PK data	References
Dendrimers	PEG-lysine	lys8(PEG200)16; 6 kDa	i.v., 5mg kg, Rats; CL 194 ± 5.4 mL h^{-1}; % ^{3}H dose in urine: 69.0 ± 17.7% at 8 h; 82.2 ± 6.4% at day 7	[97]
	PEG-lysine	lys16(PEG200)32; 11.1 kDa	i.v., 5 mg kg, Rats; CL 115 ± 4.9 mL h^{-1}; % ^{3}H dose in urine: 51.2 ± 44.4% at 8 h; 80.4 ± 13.5% at day 7	[97]
	PEG-lysine	lys16(PEG570)32, 22.4 kDa	i.v., 5 mg kg, Rats; CL 5.2 ± 0.8 mL h^{-1}; % ^{3}H dose in urine: 27.4 ± 3.4% at 8 h; 42.9 ± 2.7% at day 7	[97]
	PEG-lysine	lys8(PEG2000)16, 34.1 kDa	i.v., 5 mg kg, Rats; CL 0.9 ± 0.1 mL h^{-1}; % ^{3}H dose in urine:4.0 ± 0.5% at 8 h; 26.0 ± 4.6% at day 7	[97]
	PEG-lysine	lys16(PEG2000)32; 68 kDa	i.v., 5 mg kg, Rats; CL 0.4 ± 0.1 mL h^{-1}; % ^{3}H dose in urine: 0.6 ± 0.3% at 24 h; 3.1 ± 1.9% at day 7	[97]
	PEG-lysine	G4: (PEG570)32; MW, 22.2 kDa	i.v., mice, Vc, 13.8 ± 0.9 mL; CL, 2.7 ± 0.1 mL h^{-1}; % ^{3}H dose in urine: 32.7 ± 7.8	[145]
	PEG-lysine	G5: (PEG570)64; MW, 47.5 kDa	i.v., mice, Vc, 13.0 ± 0.6 mL; CL, 0.4 ± 0.0 mL h^{-1}; % ^{3}H dose in urine: 5.7 ± 0.5	[145]
	PEG-methotrexate	G3: (PEG570)8(MTX)8; MW, 10.5 kDa	i.v., mice, Vc, 16.2 ± 0.7 mL; CL, 133 ± 19 mL h^{-1}; % ^{3}H dose in urine: 55.7 ± 8.6	[145]
	PEG-methotrexate	G3: (PEG1100)8(MTX)8; MW, 14.8 kDa	i.v., mice, Vc, 19.6 ± 6.1 mL; CL, 98.5 ± 29.3 mL h^{-1}; % ^{3}H dose in urine: 64.1 ± 4.7	[145]
	PEG-methotrexate	G4: (PEG570)16(MTX)16; MW, 21.1 kDa	i.v., mice, Vc, 23.3 ± 1.4 mL; CL, 51.9 ± 2.3 mL h^{-1}; % ^{3}H dose excreted in urine: 29.0 ± 3.4	[145]
	PEG-methotrexate	G4: (PEG1100)16(MTX)16; MW, 29.6 kDa	i.v., mice, Vc, 14.4 ± 1.7 mL; CL, 1.4 ± 0.1 mL h^{-1}; % ^{3}H dose in urine: 23.5 ± 17.7	[145]
	PEG-methotrexate	G4: (PEG2200)16(MTX)16; MW, 47.2 kDa	i.v., mice, Vc, 13.3 ± 0.6 mL; CL, 0.6 ± 0.1 mL h^{-1}; % ^{3}H dose in urine: 8.4 ± 1.4	[145]
	PEG-methotrexate	G5: (PEG570)32(MTX)32; MW, 42.2 kDa	i.v., mice, Vc, 16.2 ± 0.1 mL; CL, 1.5 ± 0.1 mL h^{-1}; % ^{3}H dose in urine: 2.4 ± 0.5	[145]
	PEG-methotrexate	G5: (PEG1100)32(MTX)32; MW, 59.2 kDa	i.v., mice, Vc, 16.0 ± 1.1 mL; CL, 0.6 ± 0.0 mL h^{-1}; % ^{3}H dose in urine: 1.2 ± 0.1	[145]

(*continued overleaf*)

Table 1.5 (*continued*)

NM		Description	PK data	References
Organic NPs	Polymeric NP	PRINT NP; 236 nm, −27.9 mV	i.v., mice, AUC, 0.013 mg mL h; Vd, 4.75 mL; CL, 17.5 mL h^{-1}	[98]
	Polymeric NP	PEGylated (mushroom); 341 nm, −8.15 mV	i.v., mice, AUC, 1.12 mg mL h; Vd, 1.40 mL; CL, 0.128 mL h^{-1}	[98]
	Polymeric NP	PEGylated (brush); 347 nm, −11.6 mV	i.v., mice, AUC, 1.66 mg mL h; Vd, 1.48 mL; CL, 0.087 mL h^{-1}	[98]
Liposome	PEG-liposome	80 – 100 nm	i.v., mice, BD: blood, 7.98% g^{-1}; liver, 14.2% g^{-1}; spleen, 33.5% g^{-1}; kidney, 3.72% g^{-1}; lungs, 0.61% g^{-1}; heart, 0.68% g^{-1}; skin, 3.97% g^{-1}; bone, 3.50% g^{-1}; BT-474 tumor, 7.32% g^{-1} (tumor/muscle ratio, 9.9); MCF7 tumor, 8.59% g^{-1} (tumor/muscle ratio, 11.6)	[147]
	Anti-HER2-liposome	80 – 100 nm	i.v., mice, BD: blood, 7.04% g^{-1}; liver, 15.6% g^{-1}; spleen, 41.6% g^{-1}; kidney, 3.21% g^{-1}; lungs, 0.42% g^{-1}; heart, 0.58% g^{-1}; skin, 4.71% g^{-1}; bone, 2.06% g^{-1}; T-474 tumor, 8.34% g^{-1} (tumor/muscle ratio, 22.5); MCF7 tumor, 7.18% g^{-1} (tumor/muscle ratio, 19.4)	[147]
Metallic NPs	QDs	CdTe QD; 4 nm	i.v., 2.5 µmol kg^{-1}, mice, for Cd: AUC, 18.73 ± 2.29 µg mL^{-1} h; Vd, 127.25 ± 5.65 mL kg^{-1}; CL, 14.81 ± 1.90 mL kg^{-1} h^{-1}; for Te: AUC, 15.28 ± 0.89 µg mL^{-1} h; Vd, 107.41 ± 9.75 mL kg^{-1}; CL, 10.38 ± 0.80 mL kg^{-1} h^{-1}	[148]
	Ceria NPs	Ceria nanoparticle; 5 nm	i.v., rats, AUC, 2264 ± 1284 µg mL^{-1} h; C_{max}, 278 ± 215 µg mL^{-1}; MRT, 7.1 ± 3.0 h	[149]
	Ceria NPs	Ceria nanoparticle; 15 nm	i.v., rats, AUC, 361 ± 130 µg mL^{-1} h; C_{max}, 0.95 ± 0.34 µg mL^{-1}; MRT, 41 ± 11 h	[149]
	Ceria NPs	Ceria nanoparticle; 30 nm cubic nanoparticle	i.v., rats, AUC, 2201 ± 1314 µg mL^{-1} h; C_{max}, 6.5 ± 3.1 µg mL^{-1}; MRT, 15 ± 11 h	[149]
	Ceria NPs	Ceria nanoparticle; 30 nm cubic + rods	i.v., rats, AUC, 25 ± 8 µg mL^{-1} h; C_{max}, 20 ± 11 µg mL^{-1}; MRT, 1.6 ± 1.8 h	[149]

Gold NPs	Ceria nanoparticle; 50 nm	i.v., rats, AUC, $1.5 \pm 0.5\ \mu g\ mL^{-1}\ h$; C_{max}, $0.78 \pm 0.12\ \mu g\ mL^{-1}$; MRT, 1.5 ± 0.1 h	[149]
Gold NPs	Citrate-coated gold nanoparticle; 22.4 nm, -44.7 ± 7.5 mV	i.v., rats, BD at 24 h: liver, $57.94 \pm 2.57\%$; spleen, $1.34 \pm 0.23\%$; lung, $0.72 \pm 0.44\%$; blood, $1.27 \pm 0.43\%$; heart, $0.04 \pm 0.01\%$; kidney, $0.08 \pm 0.02\%$	[150]
Gold NPs	MUA-coated gold nanoparticle; 33.2 nm, -37.3 ± 8.4 mV	i.v., rats, BD at 24 h: liver, $59.37 \pm 4.08\%$; spleen, $2.26 \pm 0.52\%$; lung, $0.44 \pm 0.19\%$; blood, $1.13 \pm 0.71\%$; heart, $0.01 \pm 0.01\%$; kidney, $0.03 \pm 0.03\%$	[150]
Gold NPs	CALNN-coated gold nanoparticle; 22.4 nm, -47.1 ± 6.0 mV	i.v., rats, BD at 24 h: liver, $86.11 \pm 7.13\%$; spleen, $2.79 \pm 0.30\%$; lung, $0.53 \pm 0.06\%$; blood, $0.32 \pm 0.13\%$; heart, $0.01 \pm 0.00\%$; kidney, $0.20 \pm 0.07\%$	[150]
Gold NPs	CALND-coated gold nanoparticle; 22.4 nm, -43.6 ± 9.2 mV	i.v., rats, BD at 24 h: liver, $77.47 \pm 2.52\%$; spleen, $2.51 \pm 0.59\%$; lung, $0.88 \pm 0.6\%$; blood, $0.19 \pm 0.08\%$; heart, $0.02 \pm 0.01\%$; kidney, $0.05 \pm 0.02\%$	[150]
Gold NPs	CALNS-coated gold nanoparticle; 22.4 nm, -40.5 ± 7.0 mV	i.v., rats, BD at 24 h: liver, $73.66 \pm 4.84\%$; spleen, $1.88 \pm 0.13\%$; lung, $0.52 \pm 0.09\%$; blood, $0.38 \pm 0.07\%$; heart, $0.01 \pm 0.00\%$; kidney, $0.01 \pm 0.00\%$	[150]
Gold NPs	Triphenylphosphine-modified AuNP; 1.4 nm, -20.6 mV	i.v., 3.1 μg/rat, NP concentration at 24 h: liver, $5.1\%\ g^{-1}$; spleen, $2.3\%\ g^{-1}$; lungs, $0.2\%\ g^{-1}$; kidney, $1.9\%\ g^{-1}$; brain, $0.0064\%\ g^{-1}$; blood, $0.11\%\ g^{-1}$	[146]
Gold NPs	Triphenylphosphine-modified AuNP; 5 nm, -21.1 mV	i.v., 43.7 μg/rat, NP concentration at 24 h: liver, $10.0\%\ g^{-1}$; spleen, $2.7\%\ g^{-1}$; lungs, $0.035\%\ g^{-1}$; kidney, $0.037\%\ g^{-1}$; brain, $0.00006\%\ g^{-1}$; blood, $0.024\%\ g^{-1}$	[146]
Gold NPs	Triphenylphosphine-modified AuNP; 18 nm, -22.8 mV	i.v., 2.9 μg/rat, NP concentration at 24 h: liver, $10.0\%\ g^{-1}$; spleen, $1.6\%\ g^{-1}$; lungs, $0.038\%\ g^{-1}$; kidney, $0.013\%\ g^{-1}$; brain, $0.000031\%\ g^{-1}$; blood, $0.016\%\ g^{-1}$	[146]
Gold NPs	Triphenylphosphine-modified AuNP; 80 nm, -22.3 mV	i.v., 18.5 μg/rat, NP concentration: liver, $11\%\ g^{-1}$; spleen, $1.9\%\ g^{-1}$; lungs, $0.027\%\ g^{-1}$; kidney, $0.016\%\ g^{-1}$; brain, $0.00029\%\ g^{-1}$; blood, $0.0016\%\ g^{-1}$	[146]

(*continued overleaf*)

Table 1.5 (*continued*)

NM		Description	PK data	References
	Gold NPs	Triphenylphosphine-modified AuNP; 200 nm, −41.3 mV	i.v., 19.8 μg/rat, NP concentration: liver, 12% g^{-1}; spleen, 3.6%; lungs, 0.037% g^{-1}; kidney, 0.0025% g^{-1}; brain, 0.000021% g^{-1}; blood, 0.00086% g^{-1}	[146]
	Gold NPs	Thioglycolic acid-modified AuNP; negative	i.v., 1.6 μg/rat, NP concentration: liver, 9.2% g^{-1}; spleen, 8.9% g^{-1}; lungs, 1.2% g^{-1}; kidney, 0.4% g^{-1}; brain, 0.0018% g^{-1}; blood, 0.11% g^{-1}	[146]
	Gold NPs	Cysteamine-modified AuNP; positive	i.v., 29.0 μg/rat, NP concentration: liver, 7.9% g^{-1}; spleen, 13% g^{-1}; lungs, 1.2% g^{-1}; kidney, 0.48% g^{-1}; brain, 0.0028% g^{-1}; blood, 0.095% g^{-1}	[146]
	Silver NPs	Aqueous AgNP; 20.3 nm, 23.8 μg mL^{-1}	i.v., 23.8 μg/rat, NP concentration at 2 d: blood, 602 ± 98 ng g^{-1}; liver, 2326 ± 676 ng g^{-1}; lungs, 31 ± 11 ng g^{-1}; spleen, 38 ± 5 ng g^{-1}; brain, 8 ± 5 ng g^{-1}; heart, 7 ± 5 ng g^{-1}; kidney, 110 ± 45 ng g^{-1}; total tissue-accumulated Ag, 13 ± 3%	[151]
	Silver NPs	Aqueous AgNP; 79.8 nm, 26.4 μg mL^{-1}	i.v., 26.4 μg/rat, NP concentration at 2 d: blood, 896 ± 303 ng g^{-1}; liver, 6968 ± 3231 ng g^{-1}; lungs, 603 ± 356 ng g^{-1}; spleen, 110 ± 22 ng g^{-1}; brain, 10 ± 3 ng g^{-1}; heart, 63 ± 11 ng g^{-1}; kidney, 9 ± 1 ng g^{-1}; total tissue-accumulated Ag, 33 ± 10%	[151]
	Silver NPs	Aqueous AgNP; 112.6 nm, 27.6 μg mL^{-1}	i.v., 27.6 μg/rat, NP concentration at 2 d: blood, 582 ± 358 ng g^{-1}; liver, 13 381 ± 567 ng g^{-1}; lungs, 129 ± 60 ng g^{-1}; spleen, 859 ± 34 ng g^{-1}; brain, 8 ± 1 ng g^{-1}; heart, 11 ± 3 ng g^{-1}; kidney, 83 ± 27 ng g^{-1}; total tissue-accumulated Ag, 55 ± 0%	[151]

Table 1.6 PK variations of the encapsulated drug among different NMs.

Model drug	NM	Description	PK data	References
Paclitaxel	Chitosan NP	Chitosan/glyceryl-monooleate + paclitaxel	i.v., mice, AUC, 1.08 μg mL d^{-1} (1.46-fold); Vd, 165.8 mL; MRT, 20.49 d; tumor AUC, 132.9 ± 20.5 (20.4-fold); kp ratio for tissue/plasma was 11.6 ± 2.9 (96.9-fold)	[114]
	Chitosan NP	*N*-Octyl-*O*-sulfate chitosan micelle + paclitaxel; 200.8 nm, −28.8 mV	i.v., rats, 7 mg kg^{-1}, AUC, 3009.9 ± 877.1 μg L^{-1} h; CL, 2.49 ± 0.98 L h^{-1} kg^{-1}; MRT, 2.03 ± 0.25 h; Vd, 7.06 ± 2.89 L kg^{-1}	[115]
	PLGA NP	Peptide-PEG-PLGA loaded with paclitaxel, 120–160 nm, modified peptide may target EGFR	i.v., mice, blood PK: AUC, 497.60 μg mL^{-1} h; MRT, 2.74 h; BA increased 0.98-fold	[136]
	PLGA NP	PEG-PLGA loaded with paclitaxel; 120–160 nm, surface modified with PEG	i.v., mice, blood PK: AUC, 436.48 μg mL^{-1} h; MRT, 2.75 h; BA increased 0.86-fold	[136]
	Dendrimer	Peg5k-dendritic lysine-cholic acid (PEG5k-CA8) + paclitaxel	i.v., mice, AUC, 21 827 ng mL^{-1} h; C_{max}, 54 730 ng mL^{-1}; CL, 687 L h^{-1} kg^{-1}; Vd, 69 758 L kg^{-1}	[143]
Doxorubicin	Liposome	PEGylated liposome + dox	i.v., rats, AUC, 1786 ± 367 μg mL^{-1} h; Vd, 6.6 ± 1.5 mL; CL, 0.19 ± 0.02 mL h^{-1}; BA increased 4252.4-fold	[117]
	Liposome	PEG-liposome + dox; 100.7 nm, −20.1 mV	i.v., rats, AUC, 2183 ± 460 μg mL h; MRT, 26.96 ± 4.01 h; $t_{1/2\beta}$, 25.32 ± 4.89 h; CL 0.69 ± 0.07 mL h^{-1}; BA increased 8.3-fold	[119]
	Liposome	RGD-PEG-liposome + dox; 114.1 nm, −24.9 mV	i.v., rats, AUC, 1679 ± 189 μg mL h; MRT, 21.88 ± 0.97 h; $t_{1/2\beta}$, 24.10 ± 2.42 h; CL 1.10 ± 0.05 mL h^{-1}; BA increased 6.4-fold	[119]
	Liposome	PEGylated liposome + dox	i.v., 6 mg kg^{-1}, Mice, AUC, 2 257 480 ng mL^{-1} h; T_{max}, 3 h; C_{max}, 2181 ng mL^{-1}; BA increased 1461-fold	[120]
	Poly amido acid denderimer	PEGylated dendrimer-loaded dox via acid-labile linker; polylysine dendrimer, G 5	i.v., rats, AUC, 341 ± 39 μg mL^{-1} h; Vd, 27.5 ± 9.4 mL; CL, 0.97 ± 0.20 mL h^{-1}; BA increased 811.9-fold	[117]

and doxorubicin encapsulated by different NMs. It should be noted that conclusions should be carefully drawn based the comparison because the experimental differences exist in drug dose, administration route, animal species, sampling protocol, PK model, and the method of data analysis. A "standard protocol" should be designed to acquire the high-quality data in analyzing PK profiles of different NMs.

1.7.3 Reciprocal Blood and Tissue PK

There could be a poor correlation between drug concentrations in blood and the target organs for NM-based drug delivery. In this case, the discrepancy between blood PK and PD cannot be precisely predicted by using the conventional PK/PD model. Therefore, it is important to compare both the blood and tissue concentrations when analyzing PK of drug-loaded NMs. Table 1.7 summarizes both the blood and tissue PK from a number of NMs. It was demonstrated that the NMs with a relatively longer blood resident time were usually less efficiently taken by the major organs [152–154]. As for tumor-targeting NMs, there often was not much difference between the ligand-modified and nonmodified particles in blood PK [136], probably because of the small proportion of tumor-retained drugs.

1.7.4 PK Differences Between Different Components of the Drug-NM System

In the case of drug co-encapsulation, the PK profiles also show different behaviors for two drugs (Table 1.8). For example, the $t_{1/2}$ of the paclitaxel was less than half of the co-loaded EGCG (26.5 h vs 56.1 h) due to the intrinsic differences between the two drugs [155]. Furthermore, variations also existed between NMs and their encapsulated drugs (Table 1.9). It was found that blood PK of encapsulated Dox was different from that of the loading phospholipid, and drug $t_{1/2}$ depended on the release kinetics of the drugs from the liposomes; the liposomes with slower drug release had higher AUC [118].

1.7.5 PK Variations Among Different Routes of Administration

For intravenous administration, biodistribution of NMs is size-dependent, and rapid uptake of small NMs by the RES organs leads to a fast clearance of the loading drugs from the blood. When other types of administration (such as p.o., i.p., s.c., and i.m.) are applied, the given NMs have to penetrate a physiological membrane barrier before entering blood circulation, thereby leading to the changed PK profiles [158–160]. For the routes other than intravenous (i.v.) injection, NMs need to be carefully tailored by adopting effective strategies such as small size [134], PEGylation [121, 122], and CPP modification [132], so as to improve the blood PK of the loaded drugs (Table 1.10).

Table 1.7 Variations between blood and tissue PK of NMs or the encapsulated drugs.

NM	Description	Blood PK	Tissue PK	References
Liposome	PEGylated liposome + dox	i.v., mice; dose, 6 mg kg^{-1}; AUC, 2257.5 μg mL^{-1} h; T_{max}, 3 h; C_{max}, 2.18 μg mL^{-1}; BA increased 1461-fold	For brain tumor: AUC, 229.7 μg mL^{-1} h; BA increased 19-fold; for normal brain: AUC, 13.7 μg mL^{-1} h; BA increased 42-fold	[120]
PLGA NP	Cylindrical shape NP + docetaxel; 200 nm × 200 nm ($d \times h$); −3.4 mV	i.v., mice; AUC_{0-72h}, 134 429 ng mL^{-1} h; CL, 72 mL kg^{-1} h; Vd, 257 mL kg^{-1}; BA increased 23.1-fold	Tumor: AUC_{0-24h}, 79 644 ng mL^{-1} h (1.3-fold); T_{last}, 168 h; liver: $AUC_{0-24\,h}$, 87 255 ng mL^{-1} h (8.0-fold); T_{last}, 168 h; spleen: AUC_{0-24h}, 712 569 ng mL^{-1} h (53.6-fold); T_{last}, 168 h; lung, AUC_{0-72h}, 50 887 ng mL^{-1} h (3.7-fold); T_{last}, 168 h	[152]
PLGA NP	Cylindrical shape NP + docetaxel; 80 nm × 320 nm ($d \times h$); −3.2 mV	i.v., mice, AUC_{0-72h}, 133 462 ng mL^{-1} h; CL, 73 mL kg^{-1} h; Vd, 474 mL kg^{-1}; BA increased 23.0-fold	For tumor: AUC_{0-24h}, 95 516 ng mL^{-1} h (1.5-fold); T_{last}, 168 h; liver: AUC_{0-24h}, 64 274 ng mL^{-1} h (5.9-fold); T_{last}, 168 h; spleen: AUC_{0-24h}, 324 978 ng mL^{-1} h (24.4 fold); T_{last}, 168 h; lung, AUC_{0-72h}, 44 377 ng mL^{-1} h (3.3-fold); T_{last}, 72 h	[152]
PLGA NP	EGFR targeting peptide-PEG-PLGA loaded with paclitaxel and lonidamine; 120 – 160 nm	i.v., mice. For ptx: AUC, 497.6 μg mL^{-1} h (0.98-fold); MRT, 2.7 h; CL, 40 mL kg^{-1} h^{-1}; Vd, 110 mL kg^{-1}; for lon: AUC, 1316.0 μg mL^{-1} h (1.71-fold); MRT, 4.4-h; CL, 60 mL kg^{-1} h^{-1}; Vd, 270 mL kg^{-1}	Tumor PK, for ptx: AUC, 38.32 ± 13.14 μg mL^{-1} h; MRT, 11.45 ± 3.70 h; BA increased 8.51-fold; for lon: AUC, 49.96 ± 9.87 μg mL^{-1} h; MRT, 7.25 ± 1.38 h; BA increased 10.9-fold	[136]
PLGA NP	PEG-PLGA loaded with paclitaxel and lonidamine; 120 – 160 nm	i.v., mice. For ptx: AUC, 436.5 μg mL^{-1} h (0.86-fold); MRT, 2.75 h; CL, 50 mL kg^{-1} h^{-1}; Vd, 130 mL kg^{-1}; for lon: AUC, 992.5 μg mL^{-1} h (1.95-fold); MRT, 3.8 h; CL, 80 mL kg^{-1} h^{-1}; Vd, 300 mL kg^{-1}	Tumor PK, for ptx: AUC, 25.57 ± 9.43 μg mL^{-1} h; MRT, 7.75 ± 2.01 h; BA increased 5.69-fold; for lon: AUC, 32.09 ± 14..26 μg mL^{-1} h; MRT, 4.46 ± 1.01 h; BA increased 7.00-fold	[136]

(*continued overleaf*)

Table 1.7 (*continued*)

NM	Description	Blood PK	Tissue PK	References
Nanoemulsion	NE + chlorambucil; soybean oil, egg lecithin, cholesterol	i.v. 10 mg kg^{-1}, mice. AUC, 32.4 ± 0.1 μg mL^{-1} h; MRT, 1.3 ± 0.04 h; CL, 309 ± 16 mL kg^{-1} h^{-1}; Vss, 409 ± 15 mL kg^{-1}; BA increased 1.91-fold	AUC: liver, 7.4 ± 0.02 g^{-1} h (0.90-fold); kidney, 8.0 ± 0.03 g^{-1} h (0.72-fold); heart, 8.2 ± 0.1 g^{-1} h (0.75-fold); lungs, 12.0 ± 0.2 g^{-1} h (0.92-fold); spleen, 5.2 ± 0.3 g^{-1} h (1.24-fold)	[153]
Nanoemulsion	PEG-NE + chlorambucil; soybean oil, egg lecithin, cholesterol, DSPE-PEG2000	i.v. 10 mg kg^{-1}, mice. AUC, 45 ± 30 μg mL^{-1} h; MRT, 1.9 ± 0.1 h; CL, 221 ± 1.4 mL kg^{-1} h^{-1}; Vss, 339 ± 5.3 mL kg^{-1}; BA increased 2.65-fold	AUC: liver , 3.1 ± 0.02 g^{-1} h (0.38-fold); kidney, 7.1 ± 0.02 g^{-1} h (0.64-fold); heart, 8.0 ± 0.1 g^{-1} h (0.73-fold); lungs, 5.0 ± 0.1 g^{-1} h (0.38-fold); spleen, 1.0 ± 0.1 g^{-1} h (0.24-fold)	[153]
Cyclodextran inclusion complex	HP-β-CD and itraconazole inclusion complex	Oral, 10 mg kg^{-1}, rats. AUC, 87.29 ± 5.6 mg L^{-1} h; MRT, 1.75 ± 0.09 h; V, 0.54 ± 0.18 L kg^{-1}; CL, 0.12 ± 0.01 L kg^{-1} h^{-1} ; i.v., mice, AUC, 11 405.3 μg L^{-1} h; MRT, 3.4 h	i.v., Mice, heart: AUC, 938.3 μg L^{-1} h; MRT, 3.1 h; liver: AUC, 6000.2 μg L^{-1} h; MRT, 2.1 h; spleen: AUC, 930.4 μg L^{-1} h; MRT, 4.4 h; lung: AUC, 960.7 μg L^{-1} h; MRT, 4.0 h; kidney: AUC, 3263.5 μg L^{-1} h; MRT, 6.0 h	[154]
Liposome	Liposomal itraconazole; 264.5 nm, −73.6 mV	Oral, 10 mg kg^{-1}, rats. AUC, 155.5 ± 13.8 mg L^{-1} h; MRT, 3.98 ± 0.32 h; V, 0.38 ± 0.05 L kg^{-1}; CL, 0.06 ± 0.01 L kg^{-1} h^{-1}; i.v., mice, AUC, 18 610.9 μg L^{-1} h; MRT, 9.1 h	i.v., Mice, heart: AUC, 299.1 μg L^{-1} h; MRT, 2.0 h; liver: AUC, 11 606.7 μg L^{-1} h; MRT, 2.9 h; spleen: AUC, 3230.7 μg L^{-1} h; MRT, 9.9 h; lung: AUC, 940.7 μg L^{-1} h; MRT, 4.1h; kidney: AUC, 1306.1 μg L^{-1} h; MRT, 4.8 h	[154]
PEG-liposome	80 – 100 nm	i.v., mice, BD: blood, 7.98% g^{-1}	Liver, 14.2% g^{-1}; spleen, 33.5% g^{-1}; kidney, 3.72% g^{-1}; lungs, 0.61% g^{-1}; heart, 0.68% g^{-1}; skin, 3.97% g^{-1}; bone, 3.50% g^{-1}; BT-474 tumor, 7.32% g^{-1} (tumor/muscle ratio, 9.9); MCF7 tumor, 8.59% g^{-1} (tumor/muscle ratio, 11.6)	[147]

Anti-HER2-liposome	80–100 nm	i.v., Mice, BD: blood, 7.04% g^{-1}	Liver, 15.6% g^{-1}; spleen, 41.6% g^{-1}; kidney, 3.21% g^{-1}; lungs, 0.42% g^{-1}; heart, 0.58% g^{-1}; skin, 4.71% g^{-1}; bone, 2.06% g^{-1}; T-474 tumor, 8.34% g^{-1} (tumor/muscle ratio, 22.5); MCF7 tumor, 7.18% g^{-1} (tumor/muscle ratio, 19.4)	[147]
Lipid NP	(Soylecithin, P188, trimyristin) + clozapine; 233.3 nm, 0.2 mV	i.v., 10 mg kg^{-1}, rats, AUC, 9.67 ± 1.86 μg mL^{-1} h; CL, 1.07 ± 0.2 L h^{-1} kg^{-1}; MRT, 8.92 ± 1.28 h; BA increased 1.51-fold	AUC: kidney, 52.44 μg g^{-1} h (1.94); liver, 56.86 μg g^{-1} h (2.08); spleen, 70.85 μg g^{-1} h (4.38); heart, 44.01 μg g^{-1} h (1.65); brain: 73.69 μg g^{-1} h (4.05)	[131]
Lipid NP	(Soylecithin, P188, stearylamine, trimyristin) + clozapine; 150.2 nm, 33.2 mV	i.v., 10 mg kg^{-1}, rats, AUC, 13.72 ± 1.7 μg mL^{-1} h; CL, 0.74 ± 0.1 L h^{-1} kg^{-1}; MRT, 9.52 ± 1.85 h; BA increased 2.15-fold	AUC: kidney, 37.16 μg g^{-1} h (1.38); liver, 45.50 μg g^{-1} h (1.67); spleen, 48.35 μg g^{-1} h (2.99); heart, 36.42 μg g^{-1} h (1.36); brain: 95.78 μg g^{-1} h (5.27)	[131]
Polymeric dendrimer	G4 PAMAM + indomethacin	i.v., 3.3 mg kg^{-1}, rats, AUC, 125.9 ± 22.3 μg mL^{-1} h; C_{max}, 34.6 ± 0.6 μg mL^{-1}; CL, 0.40 ± 0.03 mL min^{-1} kg^{-1}; MRT, 5.72 ± 0.47 h; BA increased 1.37-fold	AUC: brain, 107.7μg mL^{-1} h (0.77); heart, 225.4 μg mL^{-1} h (0.59); kidney, 71.9 μg mL^{-1} h (0.75); liver, 150.3 μg mL^{-1} h (0.85); lung, 198.2 μg mL^{-1} h (0.87); spleen, 189.0 μg mL^{-1} h (0.87); for target organ, 396.4 μg mL^{-1} h (1.91)	[140]
Polymeric dendrimer	Folic acid-modified G4 PAMAM + indomethacin; folic acid : PAMAM = 3.86	i.v., 3.3 mg kg^{-1}, rats, AUC, 127.6 ± 25.2 μg mL^{-1} h; C_{max}, 28.3 ± 5.5 μg mL^{-1}; CL, 0.40 ± 0.04 mL min^{-1} kg^{-1}; MRT, 6.60 ± 0.01 h; BA increased 1.39-fold	AUC: brain, 79.0 μg mL^{-1} h (0.57); heart, 341.5 μg mL^{-1} h (0.90); kidney, 76.6 μg mL^{-1} h (0.80); liver, 183.6 μg mL^{-1} h (1.04); lung, 229.0 μg mL^{-1} h (1.00); spleen, 176.8 μg mL^{-1} h (0.81); for target organ, 579.0 μg mL^{-1} h (2.79)	[140]

(*continued overleaf*)

Table 1.7 (*continued*)

NM	Description	Blood PK	Tissue PK	References
Polymeric dendrimer	Folic acid-modified G4 PAMAM + indomethacin; folic acid: PAMAM = 11.9	i.v., 3.3 mg kg^{-1}, rats, AUC, 121.2 ± 1.9 μg mL^{-1} h; C_{max}, 18.8 ± 9.2 μg mL^{-1}; CL, 0.46 ± 0.01 mL min^{-1} kg^{-1}; MRT, 7.77 ± 1.70 h; BA increased 1.32-fold	AUC: brain, 90.0 μg mL^{-1} h (0.65); heart, 353.7 μg mL^{-1} h (0.93); kidney, 143.2 μg mL^{-1} h (1.50); liver, 195.2 μg mL^{-1} h (1.11); lung, 205.3 μg mL^{-1} h (0.90); spleen,162.9 μg mL^{-1} h (0.75); for target organ, 602.9 μg mL^{-1} h (2.91)	[140]
Polymeric dendrimer	Folic acid-modified G4 PAMAM + indomethacin; folic acid: PAMAM = 21.4	i.v., 3.3 mg kg^{-1}, rats, AUC, 166.6 ± 0.2 μg mL^{-1} h; C_{max}, 28.4 ± 1.5 μg mL^{-1}; CL, 0.33 ± 0.00 mL min^{-1} kg^{-1}; MRT, 7.03 ± 0.07 h; BA increased 1.81-fold	AUC: brain, 172.0 μg mL^{-1} h (1.30); heart, 229.9 μg mL^{-1} h (0.60); kidney, 76.6 μg mL^{-1} h (0.80); liver, 155.0 μg mL^{-1} h (0.88); lung, 182.0 μg mL^{-1} h (0.80); spleen, 119.2 μg mL^{-1} h (0.55); for target organ, 850.7 μg mL^{-1} h (4.10)	[140]
Metallic NP	Triphenylphosphine-modified AuNP; 1.4 nm, −20.6 mV	i.v., 3.1 μg/rat, NP concentration at 24 h: blood, 0.11% g^{-1}	NP concentration at 24 h: liver, 5.1% g^{-1}; spleen, 2.3% g^{-1}; lungs, 0.2% g^{-1}; kidney, 1.9% g^{-1}; brain, 0.0064% g^{-1}	[146]
Metallic NP	Triphenylphosphine-modified AuNP; 5 nm, −21.1 mV	i.v., 43.7 μg/rat, NP concentration at 24 h: blood, 0.024% g^{-1}	NP concentration at 24 h: liver, 10.0% g^{-1}; spleen, 2.7% g^{-1}; lungs, 0.035% g^{-1}; kidney, 0.037% g^{-1}; brain, 0.00006% g^{-1}	[146]
Metallic NP	Triphenylphosphine-modified AuNP; 18 nm, −22.8 mV	i.v., 2.9 μg/rat, NP concentration at 24 h: blood, 0.016% g^{-1}	NP concentration at 24 h: liver, 10.0% g^{-1}; spleen, 1.6% g^{-1}; lungs, 0.038% g^{-1}; kidney, 0.013% g^{-1}; brain, 0.000031% g^{-1}	[146]
Metallic NP	Triphenylphosphine-modified AuNP; 80 nm, −22.3 mV	i.v., 18.5 μg/rat, NP concentration: blood, 0.0016% g^{-1}	NP concentration: liver, 11% g^{-1}; spleen, 1.9% g^{-1}; lungs, 0.027% g^{-1}; kidney, 0.016% g^{-1}; brain, 0.00029% g^{-1}	[146]
Metallic NP	Triphenylphosphine-modified AuNP; 200 nm, −41.3 mV	i.v., 19.8 μg/rat, NP concentration: blood, 0.00086% g^{-1}	NP concentration: liver, 12% g^{-1}; spleen, 3.6%; lungs, 0.037% g^{-1}; kidney, 0.0025% g^{-1}; brain, 0.000021% g^{-1}	[146]

Metallic NP	Aqueous AgNP; 20.3 nm, 23.8 μg mL^{-1}	i.v., 23.8 μg/rat, NP concentration at 2 d: blood, 602 ± 98 ng g^{-1}	NP concentration at 2 d: liver, 2326 ± 676 ng g^{-1}; lungs, 31 ± 11 ng g^{-1}; spleen, 38 ± 5 ng g^{-1}; brain, 8 ± 5 ng g^{-1}; heart, 7 ± 5 ng g^{-1}; kidney, 110 ± 45 ng g^{-1}; total tissue-accumulated Ag, 13 ± 3%	[151]
Metallic NP	Aqueous AgNP; 79.8 nm, 26.4 μg mL^{-1}	i.v., 26.4 μg/rat, NP concentration at 2 d: blood, 896 ± 303 ng g^{-1}	NP concentration at 2 d: liver, 6968 ± 3231 ng g^{-1}; lungs, 603 ± 356 ng g^{-1}; spleen, 110 ± 22 ng g^{-1}; brain, 10 ± 3 ng g^{-1}; heart, 63 ± 11 ng g^{-1}; kidney, 9 ± 1 ng g^{-1}; total tissue-accumulated Ag, 33 ± 10%	[151]
Metallic NP	Aqueous AgNP; 112.6 nm, 27.6 μg mL^{-1}	i.v., 27.6 μg/rat, NP concentration at 2 d: blood, 582 ± 358 ng g^{-1}	NP concentration at 2 d: liver, 13 381 ± 567 ng g^{-1}; lungs, 129 ± 60 ng g^{-1}; spleen, 859 ± 34 ng g^{-1}; brain, 8 ± 1 ng g^{-1}; heart, 11 ± 3 ng g^{-1}; kidney, 83 ± 27 ng g^{-1}; total tissue-accumulated Ag, 55 ± 0%	[151]
Metallic NP	Citrate-coated gold NPs; 22.4 nm, −44.7 mV	i.v., rats, blood content at 24 h: 1.27 ± 0.43%	BD at 24 h: liver, 57.94 ± 2.57%; spleen, 1.34 ± 0.23%; lung, 0.72 ± 0.44%; heart, 0.04 ± 0.01%; kidney, 0.08 ± 0.02%	[150]
Metallic NP	MUA-coated gold NPs; 33.2 nm, −37.3 mV	i.v., rats, blood content at 24 h: blood, 1.13 ± 0.71%	BD at 24 h: liver, 59.37 ± 4.08%; spleen, 2.26 ± 0.52%; lung, 0.44 ± 0.19%; heart, 0.01 ± 0.01%; kidney, 0.03 ± 0.03%	[150]
Metallic NP	CALNN-coated gold NPs; 22.4 nm, −47.1 mV	i.v., rats, blood content at 24 h: blood, 0.32 ± 0.13%	BD at 24 h: liver, 86.11 ± 7.13%; spleen, 2.79 ± 0.30%; lung, 0.53 ± 0.06%; heart, 0.01 ± 0.00%; kidney, 0.20 ± 0.07%	[150]
Metallic NP	CALND-coated gold NPs; 22.4 nm, −43.6 mV	i.v., rats, blood content at 24 h: blood, 0.19 ± 0.08%	BD at 24 h: liver, 77.47 ± 2.52%; spleen, 2.51 ± 0.59%; lung, 0.88 ± 0.6%; heart, 0.02 ± 0.01%; kidney, 0.05 ± 0.02%	[150]
Metallic NP	CALNS-coated gold NP; 22.4 nm, −40.5 mV	i.v., rats, blood content at 24 h: blood, 0.38 ± 0.07%	BD at 24 h: liver, 73.66 ± 4.84%; spleen, 1.88 ± 0.13%; lung, 0.52 ± 0.09%; heart, 0.01 ± 0.00%; kidney, 0.01 ± 0.00%	[150]

Table 1.8 PK variations of the encapsulated drugs in the drug-NM systems.

NM	Description	PK data		References
		Drug 1	Drug 2	
PLGA NP	Casein-coated PLGA NP + paclitaxel and ECCG; 190 nm, with PLGA core loaded with paclitaxel, and coated casein loaded with ECCG	i.v., rats, for ptx: AUC, $179.3 \pm 34.2\,\mu g\,mL^{-1}$ h; C_{max}, $1.48 \pm 0.65\,\mu g\,mL^{-1}$; MRT, 207.7 ± 45.2 h; $t_{1/2}$, 26.5 ± 2.4 h; BA increased 8.0-fold	For EGCG: AUC, $6861.5 \pm 169.6\,\mu g\,mL^{-1}$ h; C_{max}, $119.4 \pm 6.5\,\mu g\,mL^{-1}$; MRT, 110.7 ± 33.0 h; $t_{1/2}$, 56.1 ± 11.6 h; BA increased 17.6-fold	[155]
PLGA NP	Peptide-PEG-PLGA loaded with paclitaxel and lonidamine; 120–160nm, modified peptide may target EGFR	i.v., mice, for ptx: AUC, $497.60 \pm 17.46\,\mu g\,mL^{-1}$ h (0.98-fold); MRT, 2.74 h; CL, $40\,mL\,kg^{-1}\,h^{-1}$; Vd, $110\,mL\,kg^{-1}$; tumor PK: AUC, $38.32 \pm 13.14\,\mu g\,mL^{-1}$ h (8.51-fold); MRT, 11.45 h	For lon: AUC, $1316.01 \pm 33.07\,\mu g\,mL^{-1}$ h (1.71-fold); MRT, 4.38 h; CL, $60\,mL\,kg^{-1}\,h^{-1}$; Vd, $270\,mL\,kg^{-1}$; tumor PK: AUC, $49.96 \pm 9.87\,\mu g\,mL^{-1}$ h (10.9-fold); MRT, 7.25 h	[136]
PLGA NP	PEG-PLGA loaded with paclitaxel and lonidamine; 120–160 nm, surface modified with PEG	i.v., mice. For ptx: AUC, $436.48\,\mu g\,mL^{-1}$ h (0.86-fold); MRT, 2.75 h; CL, $50\,mL\,kg^{-1}\,h^{-1}$; Vd, $130\,mL\,kg^{-1}$; tumor PK: AUC, $25.57 \pm 9.43\,\mu g\,mL^{-1}$ h (5.69-fold); MRT, 7.75 h	For lon: AUC, $992.44 \pm 35.46\,\mu g\,mL^{-1}$ h (1.95-fold); MRT, 3.77 h; CL, $80\,mL\,kg^{-1}\,h^{-1}$; Vd, 300 mL k; tumor PK: AUC, $32.09\,\mu g\,mL^{-1}$ h (7.0-fold); MRT, 4.46 h	[136]
Micelle	PEG, DSPE/TPGS mixed micelle + paclitaxel and tanespimycin; ~10 nm	i.v., mice, for ptx: AUC, $4216.8 \pm 195.0\,\mu M$ min (10.2-fold); CL_t, $5.6\,mL\,kg^{-1}\,min^{-1}$; Vd, $311.2\,mL\,kg^{-1}$	For tanespimycin: AUC, $3316.6 \pm 174.1\,\mu M$ min (3.0-fold); CL_t, $19.3\,mL\,kg^{-1}\,min^{-1}$; Vd, $468.6\,mL\,kg^{-1}$	[156]
PLGA NP	PEG-coated PLGA + rifampicin and isoniazid; 229–382 nm, 12.45 ± 4.53 mV	Oral, mice, AUC, $498.5\,\mu g\,mL^{-1}$ min (0.44 fold); C_{max}, $50.2\,\mu g\,mL^{-1}$; CL, $2.8\,mL\,min^{-1}$; MRT, 13.4 min	Oral, mice, AUC, $503.1\,\mu g\,mL^{-1}$ min (3.36-fold); C_{max}, $29.7\,\mu g\,mL^{-1}$; CL, $8.2\,mL\,min^{-1}$; MRT, 17.8 min	[157]

Table 1.9 PK variations between encapsulated drugs and other components in the drug-NM systems.

NM	Description	PK data		References
		Drug	NM component	
Liposome	CD19 antibody-modified (HSPC + cholesterol) + doxorubicin; 100 ± 10 nm	i.v., mice. For dox: AUC, 60.0 mg kg^{-1} h; $t_{1/2(CL)}$, 19.2 h; $t_{1/2(release)}$, 315.0 h	For phospholipid: AUC, 318.4 mg kg^{-1} h; $t_{1/2(CL)}$, 20.6 h	[118]
Liposome	CD19 antibody-modified (DPPC + cholesterol) + doxorubicin; 100 ± 10 nm	i.v., mice. For dox: AUC, 56.5 mg kg^{-1} h; $t_{1/2(CL)}$, 16.9 h; $t_{1/2(release)}$ 125.0 h	For phospholipid: AUC, 229.0 mg kg^{-1} h; $t_{1/2(CL)}$, 19.1 h	[118]
Liposome	CD19 antibody-modified (PMPC + cholesterol) + doxorubicin; 100 ± 10 nm	i.v., mice. For dox: AUC, 40.4 mg kg^{-1} h; $t_{1/2(CL)}$, 14.4 h; $t_{1/2(release)}$ 65.0 h	For phospholipid: AUC, 239.6 mg kg^{-1} h; $t_{1/2(CL)}$, 17.6 h	[118]
Liposome	CD19 antibody-modified (POPC + cholesterol) + doxorubicin; 100 ± 10 nm	i.v., mice. For dox: AUC, 48.8 mg kg^{-1} h; $t_{1/2(CL)}$, 13.1 h; $t_{1/2(release)}$ 40.5 h	For phospholipid: AUC, 233 mg kg^{-1} h; $t_{1/2(CL)}$, 17.7 h	[118]
Liposome	CD19 antibody-modified (DOPC + cholesterol) + doxorubicin; 100 ± 10 nm	i.v., mice. For dox: AUC, 19.5 mg kg^{-1} h; $t_{1/2(CL)}$, 7.6 h; $t_{1/2(release)}$, 1.9 h	For phospholipid: AUC, 182.0 mg kg^{-1} h; $t_{1/2(CL)}$, 15.7 h	[118]
QDs	CdTe QD; 4 nm	i.v., 2.5 μmol kg^{-1}, mice, Cd: AUC, 18.73 μg mL^{-1} h; Vd, 127.25 mL kg^{-1}; CL, 14.81 mL kg^{-1} h^{-1}	Te: AUC, 15.28 μg mL^{-1} h; Vd, 107.41 mL kg^{-1}; CL, 10.38 mL kg^{-1} h^{-1}	[148]

Table 1.10 PK variations of NMs (or encapsulated drugs) via different routes of administration.

NM	Description	PK data	References
Lipid NP	SLN + dox; 280.2 nm, but may increase to 462.3 nm in intestinal fluids	Oral, rats, C_{max}, 1.90 μg mL^{-1}; T_{max}, 1.5 h, AUC_{0-t}, 17.79 μg mL^{-1} h; MRT, 22.87 h; Ke, 0.2 h^{-1}; BA 377.7%	[121]
Lipid NP	PEGylated SLN + dox; 150.2 nm, and remains stable in intestinal fluids	Oral, C_{max}, 2.26 μg mL^{-1}; T_{max}, 0.5, 4 h, AUC_{0-t}, 35.4 μg mL^{-1} h; MRT, 33.03 h; Ke, 0.07 h^{-1}; BA 751.6%	[121]
PLGA	PLGA NP + curcumin; 161.9 nm	Rats, oral, 50 mg kg^{-1}; AUC_{0-t},134.25 ± 3.45 ng mL^{-1} h; C_{max}, 11.78 ± 0.45 ng mL; T_{max}, 2 h; Ke, 0.18 ± 0.02 h^{-1}; Vd, 2073.66 ± 352.61 L kg^{-1}; CL 365.19 ± 37.35 L kg^{-1} h^{-1}; BA increased 15.6-fold	[122]
PLGA	PEG-PLGA + curcumin; 152.4 nm	Rats, oral, 50 mg kg^{-1}; AUC_{0-t}, 447.80 ± 64.03 ng mL^{-1} h; C_{max}, 29.78 ± 4.63 ng mL; T_{max}, 3 h; Ke, 0.18 ± 0.02 h^{-1}; Vd, 900.54 ± 225.77 L kg^{-1}; CL 103.679 ± 10.90 L kg^{-1} h^{-1}; BA increased 55.5-fold	[122]
Drug NP	Atorvastatin calcium NP; 123 nm	Oral, rats; AUC_{0-12h}, 3688 ± 269 ng mL^{-1} h; C_{max}, 1454 ± 166 ng mL^{-1}; T_{max}, 1.0 ± 0 h; MRT, 3.4 ± 0.4 h; BA increased 2.1-fold	[161]
Drug NP	Atorvastatin calcium NP; 181 nm	Oral, rats; AUC_{0-12h}, 3305 ± 136 ng mL^{-1} h; C_{max}, 1145 ± 107 ng mL^{-1}; T_{max}, 1.1 ± 0.2 h; MRT, 3.6 ± 0.3 h; BA increased 1.9-fold	[161]
Drug NP	Atorvastatin calcium NP; 453 nm	Oral, rats; AUC_{0-12h}, 2846 ± 133 ng mL^{-1} h; C_{max}, 986 ± 64 ng mL^{-1}; T_{max}, 1.2 ± 0.3 h; MRT, 3.6 ± 0.3 h; BA increased 1.6-fold	[161]
Lipid NP	CTAB-coated lipid nanocapsule + fondaparinux; 58.2 nm, 42.9 mV	Oral, 5 mg kg^{-1}, rats. AUC, 336.5 ± 187.3 μg mL^{-1} min; MRT, 177.1 ± 82.6 min; CL, 450.7 ± 7.1 mL min^{-1}; C_{max}, 0.98 ± 0.33 mL^{-1}; BA increased 6.9-fold	[129]
Lipid NP	Stearylamine-coated lipid nanocapsule + fondaparinux; 48.1 nm, 4.0 mV	Oral, 5 mg kg^{-1}, rats. AUC, 730.9 ± 214.9 μg mL^{-1} min; MRT, 338.4 ± 69.4 min; CL, 485.9 ± 13.8 mL min^{-1}; C_{max}, 1.31 ± 0.37 mL^{-1}; BA increased 15.0-fold	[129]
Dendrimer	PAMAM G0 + calcitonin; 1% PAMAM	Pulmonary absorption, rats. PA%, 22.0 ± 0.8% (2.3-fold)	[141]
Dendrimer	PAMAM G1 + calcitonin; 1% PAMAM	Pulmonary absorption, rats. PA%, 23.7 ± 0.7% (2.4-fold)	[141]
Dendrimer	PAMAM G2 + calcitonin; 1% PAMAM	Pulmonary absorption, rats. PA%, 25.0 ± 2.7% (2.6-fold)	[141]

Dendrimer	PAMAM G3 + calcitonin; 1% PAMAM	Pulmonary absorption, rats. PA%, 27.6 ± 1.6% (2.8-fold)	[141]
Lipid NP	SLN (Precirol ATO-5, Labrafil M 1944CS) + tripterine; 102.4 nm, −26.2 mV	Oral, dogs, AUC, 1792.0 ± 57.1 μg L^{-1} h; C_{max}, 305.0 ± 35.4 μg L^{-1}; $t_{1/2}$, 3.85 ± 0.94 h; MRT, 4.37 ± 0.33 h; BA increased 2.86-fold	[132]
Lipid NP	CPP-modified SLN (Precirol ATO-5, Labrafil M 1945CS) + tripterine; 126.7 nm, 28.7 mV	Oral, dogs, AUC, 2568.0 ± 343.4 μg L^{-1} h; C_{max}, 483.0 ± 15.4 μg L^{-1}; $t_{1/2}$, 3.09 ± 0.54 h; MRT, 4.08 ± 0.37 h; BA increased 4.10-fold	[132]
Chitosan NP	PVP-chitosan NP + norcantharidin; 140.0 nm, 12.3 mV	Oral, 5 mg kg^{-1}, rats; AUC, 6.68 ± 1.08 μg mL^{-1} h; MRT, 6.53 ± 3.42 h; Vd, 6.52 ± 3.87 L kg^{-1}; BA increased 1.7-fold	[158]
Chitosan NP	PVP-chitosan NP + norcantharidin; 140.0 nm, 12.3 mV	i.v., 5 mg kg^{-1}, rats; AUC, 32.90 ± 4.63 μg mL^{-1} h; MRT, 0.93 ± 0.21 h; Vd, 0.62 ± 0.26 L kg^{-1}; BA increased 3.1-fold	[158]
Polymeric nanogel	Cholesteryl-hyaluronic acid gel + curcumin; 20 nm	i.v., 1.75 mg kg^{-1}, mice. AUC, 16 830 ± 1111 ng mL^{-1} h; CL, 2.08 ± 0.14 mL h^{-1}; MRT, 8.51 ± 0.52 h	[159]
Polymeric nanogel	Cholesteryl-hyaluronic acid gel + curcumin; 20 nm	i.p., 1.75 mg kg^{-1}, mice. AUC, 16 686 ± 1018 ng mL^{-1} h; CL, 2.10 ± 0.13 mL h^{-1}; MRT, 8.58 ± 0.62 h	[159]
Polymeric nanogel	Cholesteryl-hyaluronic acid gel + curcumin; 20 nm	p.o., 1.75 mg kg^{-1}, mice. AUC, 11 503 ± 843 ng mL^{-1} h; CL, 3.17 ± 0.24 mL h^{-1}; MRT, 8.95 ± 0.51 h	[159]
Lipid NP	SLN + praziquantel; 344 nm	Oral, mice. AUC, 61.0 ± 2.7 mg L^{-1} h; C_{max}, 1.1 ± 0.1 μg mL^{-1}; MRT, 95.9 ± 4.3 h; BA increased 14.8-fold	[160]
Lipid NP	SLN + praziquantel; 344 nm	s.c., mice. AUC, 101.6 ± 9.2 mg L^{-1} h; C_{max}, 1.4 ± 0.1 μg mL^{-1}; MRT, 151.6 ± 9.3 h; BA increased 16.0-fold	[160]
Lipid NP	SLN + praziquantel; 344 nm	i.m., mice. AUC, 26.2 ± 1.3 mg L^{-1} h; C_{max}, 2.7 ± 0.2 μg mL^{-1}; MRT, 48.2 ± 6.8 h; BA increased 2.6-fold	[160]
Polyanhydride NP	NP + paclitaxel; 177 nm, −44.2 mV	Oral, rats, AUC, 7.4 ± 0.9 μg mL^{-1} h; C_{max}, 0.2 ± 0.0 μg mL^{-1}; MRT, 31 ± 1 h; $t_{1/2}$, 27 ± 1 h	[134]
Polyanhydride NP	PEG2k-NP + paclitaxel; 178 nm, −40.3 mV	Oral, rats, AUC, 56 ± 3 μg mL^{-1} h; C_{max}, 2.1 ± 0.1 μg mL^{-1}; MRT, 26 ± 1 h; $t_{1/2}$, 9.3 ± 0.5 h	[134]
Polyanhydride NP	PEG6k-NP + paclitaxel; 180 nm, −39.5 mV	Oral, rats, AUC, 32 ± 2 μg mL^{-1} h; C_{max}, 1.9 ± 0.1 μg mL^{-1}; MRT, 27 ± 1 h; $t_{1/2}$, 6.2 ± 0.3 h	[134]
Polyanhydride NP	PEG10k-NP + paclitaxel; 188 nm, −41.1 mV	Oral, rats, AUC, 13 ± 1 μg mL^{-1} h; C_{max}, 1.4 ± 0.1 μg mL^{-1}; MRT, 18 ± 1 h; $t_{1/2}$, 29 ± 2 h	[134]

1.8 Perspectives

1.8.1 Development of NMs

The development of NMs has raised great attentions. NMs can improve the drug stability and protect drugs from enzymatic digestion, and enhance the bioavailability. The targeting delivery and controlled release of the NM-encapsulated drugs are also beneficial for cancer treatment and diagnosis.

However, there are many biological barriers in the human body against exogenous particles, and the majority of the administrated NMs will end up in the RES system. One of the design strategies is to escape the surveillance of the RES system by using surface modification. Moreover, targeting ligands are also used to modify the NMs to increase the specific binding with the desired organs/cells. Although much effort has been made, the overall efficiency is still under satisfaction for clinical use. The efficiency of the NM-based delivery systems needs to be further improved.

1.8.2 Pharmacokinetic Study and Model Development

The currently available pharmacokinetic studies of NMs focus on the biodistribution models. The drawback lies in the fact that the parameters such as tissue drug concentrations are hard to be detected continuously. As consequence, the limited, discontinuous data make it difficult to depict the detailed and precise PK profiles for the NMs. Compared with organ distribution, blood concentration is more convenient to determine, but the results from blood PK analysis are less suitable for NM-based systems, which are intended for an organ-specific delivery. Furthermore, the diversity of intrinsic features of NMs, modification, and species variation contribute to deviations of the overall PK behaviors of NMs. Therefore, "standard protocols" for PK experiments, including administration, dosing, sampling, and data processing, would be helpful to acquire high-quality parameters to develop PK models. A potential solution to the NM-based drug PK model could be the establishment of a theoretical "body," which is composed of different "digital" compartments simulating the physiological features of each organ. The model would help us to give better predictions on the in vivo behaviour of the NMs.

References

1. Feynman, R.P. (1960) "There's plenty of room at the bottom" an invitation to open up a new field of physics. *Eng. Sci.*, **23**, 22–36.
2. Roduner, E. (2006) Size matters: why nanomaterials are different. *Chem. Soc. Rev.*, **35**, 583–592.

3. Matsumura, Y. and Maeda, H. (1986) A new concept for macromolecular therapeutics in cancer chemotherapy: mechanism of tumoritropic accumulation of proteins and the antitumor agent smancs. *Cancer Res.*, **46**, 6387–6392.
4. Maeda, H., Takeshita, J., and Kanamaru, R. (1979) A lipophilic derivative of neocarzinostatin. A polymer conjugation of an antitumor protein antibiotic. *Int. J. Pept. Protein Res.*, **14**, 81–87.
5. Tanaka, T., Shiramoto, S., Miyashita, M., Fujishima, Y., and Kaneo, Y. (2004) Tumor targeting based on the effect of enhanced permeability and retention (EPR) and the mechanism of receptor-mediated endocytosis (RME). *Int. J. Pharm.*, **277**, 39–61.
6. Byrne, J.D., Betancourt, T., and Brannon-Peppas, L. (2008) Active targeting schemes for nanoparticle systems in cancer therapeutics. *Adv. Drug Delivery Rev.*, **60**, 1615–1626.
7. Shaikh, J., Ankola, D.D., Beniwal, V., Singh, D., and Kumar, M.N. (2009) Nanoparticle encapsulation improves oral bioavailability of curcumin by at least 9-fold when compared to curcumin administered with piperine as absorption enhancer. *Eur. J. Pharm. Sci.*, **37**, 223–230.
8. Wong, C., Stylianopoulos, T., Cui, J., Martin, J., Chauhan, V.P., Jiang, W., Popovic, Z., Jain, R.K., Bawendi, M.G., and Fukumura, D. (2011) Multistage nanoparticle delivery system for deep penetration into tumor tissue. *Proc. Natl. Acad. Sci. U.S.A.*, **108**, 2426–2431.
9. Siissalo, S., de Waard, H., de Jager, M.H., Hayeshi, R., Frijlink, H.W., Hinrichs, W.L., Dinter-Heidorn, H., van Dam, A., Proost, J.H., Groothuis, G.M., and de Graaf, I.A. (2013) Nanoparticle formulation of a poorly soluble cannabinoid receptor 1 antagonist improves absorption by rat and human intestine. *Drug Metab. Dispos.*, **41**, 1557–1565.
10. Fahr, A. and Liu, X. (2007) Drug delivery strategies for poorly water-soluble drugs. *Expert Opin. Drug Delivery*, **4**, 403–416.
11. Mager, D.E., Mody, V., Xu, C., Forrest, A., Lesniak, W.G., Nigavekar, S.S., Kariapper, M.T., Minc, L., Khan, M.K., and Balogh, L.P. (2012) Physiologically based pharmacokinetic model for composite nanodevices: effect of charge and size on in vivo disposition. *Pharm. Res.*, **29**, 2534–2542.
12. Kibria, G., Hatakeyama, H., Ohga, N., Hida, K., and Harashima, H. (2013) The effect of liposomal size on the targeted delivery of doxorubicin to Integrin alphavbeta3-expressing tumor endothelial cells. *Biomaterials*, **34**, 5617–5627.
13. Gao, Y. and Tang, Z. (2011) Design and application of inorganic nanoparticle superstructures: current status and future challenges. *Small*, **7**, 2133–2146.
14. Murakami, T. and Tsuchida, K. (2008) Recent advances in inorganic nanoparticle-based drug delivery systems. *Mini Rev. Med. Chem.*, **8**, 175–183.
15. Kwon, Y.M., Chung, H.S., Moon, C., Yockman, J., Park, Y.J., Gitlin, S.D., David, A.E., and Yang, V.C. (2009) L-Asparaginase encapsulated intact erythrocytes for treatment of acute lymphoblastic leukemia (ALL). *J. Controlled Release*, **139**, 182–189.
16. Huang, B., Tabata, Y., and Gao, J.Q. (2012) Mesenchymal stem cells as therapeutic agents and potential targeted gene delivery vehicle for brain diseases. *J. Controlled Release*, **162**, 464–473.
17. Fujihara, A., Kurooka, M., Miki, T., and Kaneda, Y. (2008) Intratumoral injection of inactivated Sendai virus particles elicits strong antitumor activity by enhancing local CXCL10 expression and systemic NK cell activation. *Cancer Immunol. Immunother.*, **57**, 73–84.
18. Ziegler, A., Nervi, P., Durrenberger, M., and Seelig, J. (2005) The cationic cell-penetrating peptide Cpp(TAT) derived from the HIV-1 protein TAT is rapidly transported into living fibroblasts: optical, biophysical, and metabolic evidence. *Biochemistry-US*, **44**, 138–148.
19. Cai, S., Yang, Q.H., Bagby, T.R., and Forrest, M.L. (2011) Lymphatic drug delivery using engineered liposomes

and solid lipid nanoparticles. *Adv. Drug Delivery Rev.*, **63**, 901–908.

20. Guo, Q.Q., Wang, H.Y., Zhao, Y.X., Wang, H.X., Zeng, F., Hua, H.Y., Xu, Q., and Huang, Y.Z. (2013) Cell-penetrating albumin conjugates for enhanced doxorubicin delivery. *Polym. Chem.-UK*, **4**, 4584–4587.
21. Cormode, D.P., Fisher, E.A., Stroes, E.S.G., Mulder, W.J.M., and Fayad, Z.A. (2013) High-density lipoprotein is a nanoparticle, but not all nanoparticles are high-density lipoprotein. *Proc. Natl. Acad. Sci. U.S.A.*, **110**, E3548.
22. Zhang, Z.H., Wang, X.P., Ayman, W.Y., Munyendo, W.L.L., Lv, H.X., and Zhou, J.P. (2013) Studies on lactoferrin nanoparticles of gambogic acid for oral delivery. *Drug Delivery*, **20**, 86–93.
23. Budin, I., Prwyes, N., Zhang, N., and Szostak, J.W. (2014) Chain-length heterogeneity allows for the assembly of fatty acid vesicles in dilute solutions. *Biophys. J.*, **107**, 1582–1590.
24. Jaworska, M., Sikora, E., and Ogonowski, J. (2014) Nanoemulsions. Characteristics and methods for preparation. *Przem. Chem.*, **93**, 1087–1092.
25. YashRoy, R.C. (1994) Destabilisation of lamellar dispersion of thylakoid membrane lipids by sucrose. *Biochim. Biophys. Acta*, **1212**, 129–133.
26. Mehnert, W. and Mäder, K. (2001) Solid lipid nanoparticles: production, characterization and applications. *Adv. Drug Delivery Rev.*, **47**, 165–196.
27. Joseph, S. and Bunjes, H. (2012) Preparation of nanoemulsions and solid lipid nanoparticles by premix membrane emulsification. *J. Pharm. Sci.-US*, **101**, 2479–2489.
28. Qiao, N., Liu, Q., Meng, H., and Zhao, D.Y. (2014) Haemolytic activity and adjuvant effect of soyasaponins and some of their derivatives on the immune responses to ovalbumin in mice. *Int. Immunopharmacol.*, **18**, 333–339.
29. Analoui, M. (2011) Nanomedicine and NanoDiagnostics: Innovation, Regulation, and Investment.
30. Sripriyalakshmi, S., Anjali, C.H., George, P.D., Rajith, B., and Ravindran, A. (2014) BSA nanoparticle loaded atorvastatin calcium – a new facet for an old drug. *PLoS One*, **9**, e86317.
31. Du, C., Deng, D., Shan, L., Wan, S., Cao, J., Tian, J., Achilefu, S., and Gu, Y. (2013) A pH-sensitive doxorubicin prodrug based on folate-conjugated BSA for tumor-targeted drug delivery. *Biomaterials*, **34**, 3087–3097.
32. Karewicz, A., Bielska, D., and Nowakowska, M. (2012) Modified polysaccharides as versatile materials in controlled delivery of antidegenerative agents. *Curr. Pharm. Des.*, **18**, 2518–2535.
33. Nakai, T., Hirakura, T., Sakurai, Y., Shimoboji, T., Ishigai, M., and Akiyoshi, K. (2012) Injectable hydrogel for sustained protein release by salt-induced association of hyaluronic acid nanogel. *Macromol. Biosci.*, **12**, 475–483.
34. Song, Y.B., Zhou, Y., and Chen, L.Y. (2012) Wood cellulose-based polyelectrolyte complex nanoparticles as protein carriers. *J. Mater. Chem.*, **22**, 2512–2519.
35. Wang, Y., Chen, H., Liu, Y., Wu, J., Zhou, P., Wang, Y., Li, R., Yang, X., and Zhang, N. (2013) pH-sensitive pullulan-based nanoparticle carrier of methotrexate and combretastatin A4 for the combination therapy against hepatocellular carcinoma. *Biomaterials*, **34**, 7181–7190.
36. Kato, Y., Ozawa, S., Miyamoto, C., Maehata, Y., Suzuki, A., Maeda, T., and Baba, Y. (2013) Acidic extracellular microenvironment and cancer. *Cancer Cell Int.*, **13**, 89.
37. Wiseman, J.W., Goddard, C.A., McLelland, D., and Colledge, W.H. (2003) A comparison of linear and branched polyethylenimine (PEI) with DCChol/DOPE liposomes for gene delivery to epithelial cells in vitro and in vivo. *Gene Ther.*, **10**, 1654–1662.
38. Chen, H.L., Liu, R., Nan, W.B., Wang, Y.X., Wang, Y.S., Yang, W.C., and Yang, W.C. (2013) Surface modification of epirubicin-loaded PLGA nanoparticle with biotinylated chitosan enhances anti-cancer efficacy in breast cancer cells. *Cancer Res.*, **73**, 5659.

39. Li, J.Q., Pu, Y.D., Wang, S.L., Ding, M.Z., Chen, D.L., and Zhu, M.D. (2013) Pharmacokinetic study and effectiveness evaluation of slow-release PLGA-5-fluorouracil microsphere. *Cancer Chemother. Pharmacol.*, **71**, 351–359.
40. Ling, T., Yu, M.F., Weng, W.J., Wang, H.M., Cheng, K., Lin, J., and Du, P.Y. (2013) Improvement of drug elution in thin mineralized collagen coatings with PLGA-PEG-PLGA micelles. *J. Biomed. Mater. Res. Part A*, **101**, 3256–3265.
41. Nounou, M.M., El-Khordagui, L.K., Khalafallah, N.A., and Khalil, S.A. (2006) In vitro release of hydrophilic and hydrophobic drugs from liposomal dispersions and gels. *Acta Pharm.*, **56**, 311–324.
42. Freeman, E.C., Weiland, L.M., and Meng, W.S. (2013) Modeling the proton sponge hypothesis: examining proton sponge effectiveness for enhancing intracellular gene delivery through multiscale modeling. *J. Biomater. Sci., Polym. Ed.*, **24**, 398–416.
43. Bandyopadhyay, S., Xia, X., Maiseiyeu, A., Mihai, G., Rajagopalan, S., and Bong, D. (2012) Z-group ketone chain transfer agents for RAFT polymer nanoparticle modification via hydrazone conjugation. *Macromolecules*, **45**, 6766–6773.
44. Shi, M., Yu, B., Gao, H., Mu, J., and Ji, C. (2013) Matrix metalloproteinase 2 overexpression and prognosis in colorectal cancer: a meta-analysis. *Mol. Biol. Rep.*, **40**, 617–623.
45. Reis, S.T., Leite, K.R., Piovesan, L.F., Pontes-Junior, J., Viana, N.I., Abe, D.K., Crippa, A., Moura, C.M., Adonias, S.P., Srougi, M., and Dall'Oglio, M.F. (2012) Increased expression of MMP-9 and IL-8 are correlated with poor prognosis of Bladder Cancer. *BMC Urol.*, **12**, 18.
46. Liu, Y., Bajjuri, K.M., Liu, C., and Sinha, S.C. (2012) Targeting cell surface alpha(v)beta(3) integrin increases therapeutic efficacies of a legumain protease-activated auristatin prodrug. *Mol. Pharmaceutics*, **9**, 168–175.
47. Yang, J. (2012) Stimuli-responsive drug delivery systems. *Adv. Drug Delivery Rev.*, **64**, 965–966.
48. Tan, L., Huang, C., Peng, R., Tang, Y., and Li, W. (2014) Development of hybrid organic–inorganic surface imprinted Mn-doped ZnS QDs and their application as a sensing material for target proteins. *Biosens. Bioelectron.*, **61**, 506–511.
49. Wong, O.A., Hansen, R.J., Ni, T.W., Heinecke, C.L., Compel, W.S., Gustafson, D.L., and Ackerson, C.J. (2013) Structure–activity relationships for biodistribution, pharmacokinetics, and excretion of atomically precise nanoclusters in a murine model. *Nanoscale*, **5**, 10525–10533.
50. Cho, E.C., Glaus, C., Chen, J., Welch, M.J., and Xia, Y. (2010) Inorganic nanoparticle-based contrast agents for molecular imaging. *Trends Mol. Med.*, **16**, 561–573.
51. Tojo, A. and Kinugasa, S. (2012) Mechanisms of glomerular albumin filtration and tubular reabsorption. *Int. J. Nephrol.*, **2012**, 481520.
52. Kapoor, A., Simmonds, P., Gerold, G., Qaisar, N., Jain, K., Henriquez, J.A., Firth, C., Hirschberg, D.L., Rice, C.M., Shields, S., and Lipkin, W.I. (2011) Characterization of a canine homolog of hepatitis C virus. *Proc. Natl. Acad. Sci. U.S.A.*, **108**, 11608–11613.
53. Lu, Y., Wang, Z.H., Li, T., McNally, H., Park, K., and Sturek, M. (2014) Development and evaluation of transferrin-stabilized paclitaxel nanocrystal formulation. *J. Controlled Release*, **176**, 76–85.
54. Alvarez-Lorenzo, C. and Concheiro, A. (2014) Smart drug delivery systems: from fundamentals to the clinic. *Chem. Commun. (Camb.)*, **50**, 7743–7765.
55. Ernsting, M.J., Murakami, M., Roy, A., and Li, S.D. (2013) Factors controlling the pharmacokinetics, biodistribution and intratumoral penetration of nanoparticles. *J. Controlled Release*, **172**, 782–794.
56. Bae, Y.H. and Park, K. (2011) Targeted drug delivery to tumors: myths, reality and possibility. *J. Controlled Release*, **153**, 198.
57. Prabhakar, U., Maeda, H., Jain, R.K., Sevick-Muraca, E.M., Zamboni, W., Farokhzad, O.C., Barry, S.T., Gabizon,

A., Grodzinski, P., and Blakey, D.C. (2013) Challenges and key considerations of the enhanced permeability and retention effect for nanomedicine drug delivery in oncology. *Cancer Res.*, **73**, 2412–2417.

58. Alexis, F., Pridgen, E., Molnar, L.K., and Farokhzad, O.C. (2008) Factors affecting the clearance and biodistribution of polymeric nanoparticles. *Mol. Pharmaceutics*, **5**, 505–515.
59. Kuo, Y.C. and Wang, L.J. (2014) Transferrin-grafted catanionic solid lipid nanoparticles for targeting delivery of saquinavir to the brain. *J. Taiwan Inst. Chem. Eng.*, **45**, 755–763.
60. Wang, Y.P., Jiang, Y.F., Zhang, M., Tan, J., Liang, J.M., Wang, H.X., Li, Y.P., He, H.N., Yang, V.C., and Huang, Y.Z. (2014) Protease-activatable hybrid nanoprobe for tumor imaging. *Adv. Funct. Mater.*, **24**, 5443–5453.
61. Buser, K., Joncourt, F., Altermatt, H.J., Bacchi, M., Oberli, A., and Cerny, T. (1997) Breast cancer: pretreatment drug resistance parameters (GSH-system, ATase, P-glycoprotein) in tumor tissue and their correlation with clinical and prognostic characteristics. *Ann. Oncol.*, **8**, 335–341.
62. Mo, R., Sun, Q., Xue, J.W., Li, N., Li, W.Y., Zhang, C., and Ping, Q.N. (2012) Multistage pH-responsive liposomes for mitochondrial-targeted anticancer drug delivery. *Adv. Mater.*, **24**, 3659–3665.
63. Lim, J., Kim, J., Duong, T., Lee, G., Kim, J., Yoon, J., Kim, J., Kim, H., Ruley, H.E., El-Rifai, W., and Jo, D. (2012) Antitumor activity of cell-permeable p18(INK4c) with enhanced membrane and tissue penetration. *Mol. Ther.*, **20**, 1540–1549.
64. Zhang, J., Shin, M.C., and Yang, V.C. (2014) Magnetic targeting of novel heparinized iron oxide nanoparticles evaluated in a 9L-glioma mouse model. *Pharm. Res.*, **31**, 579–592.
65. Gormley, A.J., Greish, K., Ray, A., Robinson, R., Gustafson, J.A., and Ghandehari, H. (2011) Gold nanorod mediated plasmonic photothermal therapy: a tool to enhance macromolecular delivery. *Int. J. Pharm.*, **415**, 315–318.
66. Shen, M., Huang, Y., Han, L., Qin, J., Fang, X., Wang, J., and Yang, V.C. (2012) Multifunctional drug delivery system for targeting tumor and its acidic microenvironment. *J. Controlled Release*, **161**, 884–892.
67. Ploegh, H.L. (2013) Logic of the immune system. *Cancer Immunol. Res.*, **1**, 5–10.
68. Podila, R., Chen, R., Ke, P.C., Brown, J.M., and Rao, A.M. (2012) Effects of surface functional groups on the formation of nanoparticle-protein corona. *Appl. Phys. Lett.*, **101**, 263701.
69. Song, G., Wu, H., Yoshino, K., and Zamboni, W.C. (2012) Factors affecting the pharmacokinetics and pharmacodynamics of liposomal drugs. *J. Liposome Res.*, **22**, 177–192.
70. Dziendzikowska, K., Gromadzka-Ostrowska, J., Lankoff, A., Oczkowski, M., Krawczynska, A., Chwastowska, J., Sadowska-Bratek, M., Chajduk, E., Wojewodzka, M., Dusinska, M., and Kruszewski, M. (2012) Time-dependent biodistribution and excretion of silver nanoparticles in male Wistar rats. *J. Appl. Toxicol.*, **32**, 920–928.
71. Yuan, F., Dellian, M., Fukumura, D., Leunig, M., Berk, D.A., Torchilin, V.P., and Jain, R.K. (1995) Vascular permeability in a human tumor xenograft: molecular size dependence and cutoff size. *Cancer Res.*, **55**, 3752–3756.
72. Fang, J., Nakamura, H., and Maeda, H. (2011) The EPR effect: unique features of tumor blood vessels for drug delivery, factors involved, and limitations and augmentation of the effect. *Adv. Drug Delivery Rev.*, **63**, 136–151.
73. Ha, S.Y., Lee, J., Jang, J., Hong, J.Y., Do, I.G., Park, S.H., Park, J.O., Choi, M.G., Sohn, T.S., Bae, J.M., Kim, S., Kim, M., Kim, S., Park, C.K., Kang, W.K., and Kim, K.M. (2014) HER2-positive gastric cancer with concomitant MET and/or EGFR overexpression: a distinct subset of patients for dual inhibition therapy. *Int. J. Cancer*, **136**, 1629–1635.
74. Malla, R.R., Gopinath, S., Alapati, K., Gorantla, B., Gondi, C.S., and Rao, J.S. (2013) Knockdown of cathepsin B and uPAR inhibits CD151 and alpha 3 beta

1 integrin-mediated cell adhesion and invasion in glioma. *Mol. Carcinog.*, **52**, 777–790.

75. Cagle, P.T., Zhai, Q.H., Murphy, L., and Low, P.S. (2013) Folate receptor in adenocarcinoma and squamous cell carcinoma of the lung potential target for folate-linked therapeutic agents. *Arch. Pathol. Lab. Med.*, **137**, 241–244.

76. Yhee, J.Y., Lee, S.J., Lee, S., Song, S., Min, H.S., Kang, S.W., Son, S., Jeong, S.Y., Kwon, I.C., Kim, S.H., and Kim, K. (2013) Tumor-targeting transferrin nanoparticles for systemic polymerized siRNA delivery in tumor-bearing mice. *Bioconjugate Chem.*, **24**, 1850–1860.

77. Xuan, C., Steward, K.K., Timmerman, J.M., and Morrison, S.L. (2010) Targeted delivery of interferon-alpha via fusion to anti-CD20 results in potent antitumor activity against B-cell lymphoma. *Blood*, **115**, 2864–2871.

78. Weiss, I., Trope, C.G., Reich, R., and Davidson, B. (2012) Hyaluronan synthase and hyaluronidase expression in serous ovarian carcinoma is related to anatomic site and chemotherapy exposure. *Int. J. Mol. Sci.*, **13**, 12925–12938.

79. Wang, Y. and Grainger, D. (2014) Barriers to advancing nanotechnology to better improve and translate nanomedicines. *Front. Chem. Sci. Eng.*, **8**, 265–275.

80. Hirsh, S.L., McKenzie, D.R., Nosworthy, N.J., Denman, J.A., Sezerman, O.U., and Bilek, M.M.M. (2013) The Vroman effect: competitive protein exchange with dynamic multilayer protein aggregates. *Colloids Surf., B*, **103**, 395–404.

81. Bertrand, N. and Leroux, J.C. (2012) The journey of a drug-carrier in the body: an anatomo-physiological perspective. *J. Controlled Release*, **161**, 152–163.

82. Kwon, I.K., Lee, S.C., Han, B., and Park, K. (2012) Analysis on the current status of targeted drug delivery to tumors. *J. Controlled Release*, **164**, 108–114.

83. Jalali, S., Huang, Y., Dumont, D.J., and Hynynen, K. (2010) Focused ultrasound-mediated bbb disruption is associated with an increase in activation of AKT: experimental study in rats. *BMC Neurol.*, **10**, 114.

84. Wang, B., He, X., Zhang, Z., Zhao, Y., and Feng, W. (2013) Metabolism of nanomaterials in vivo: blood circulation and organ clearance. *Acc. Chem. Res.*, **46**, 761–769.

85. Heurtault, B., Saulnier, P., Pech, B., Proust, J.E., and Benoit, J.P. (2003) Physico-chemical stability of colloidal lipid particles. *Biomaterials*, **24**, 4283–4300.

86. Devine, D.V., Wong, K., Serrano, K., Chonn, A., and Cullis, P.R. (1994) Liposome-complement interactions in rat serum: implications for liposome survival studies. *Biochim. Biophys. Acta*, **1191**, 43–51.

87. Hardison, W.G.M., Lowe, P.J., and Shanahan, M. (1989) Effect of molecular charge on para- and transcellular access of horseradish peroxidase into rat bile. *Hepatology*, **9**, 866–871.

88. Xiao, K., Li, Y., Luo, J., Lee, J.S., Xiao, W., Gonik, A.M., Agarwal, R.G., and Lam, K.S. (2011) The effect of surface charge on in vivo biodistribution of PEG-oligocholic acid based micellar nanoparticles. *Biomaterials*, **32**, 3435–3446.

89. Huang, X., Li, L., Liu, T., Hao, N., Liu, H., Chen, D., and Tang, F. (2011) The shape effect of mesoporous silica nanoparticles on biodistribution, clearance, and biocompatibility in vivo. *ACS Nano*, **5**, 5390–5399.

90. Snyder, G.K. and Sheafor, B.A. (1999) Red blood cells: centerpiece in the evolution of the vertebrate circulatory system. *Am. Zool.*, **39**, 189–198.

91. Gaucher, G., Asahina, K., Wang, J., and Leroux, J.C. (2009) Effect of poly(*N*-vinyl-pyrrolidone)-block-poly(D,L-lactide) as coating agent on the opsonization, phagocytosis, and pharmacokinetics of biodegradable nanoparticles. *Biomacromolecules*, **10**, 408–416.

92. Malfatti, M.A., Palko, H.A., Kuhn, E.A., and Turteltaub, K.W. (2012) Determining the pharmacokinetics and long-term biodistribution of SiO_2 nanoparticles in vivo using accelerator mass spectrometry. *Nano Lett.*, **12**, 5532–5538.

93. Morishita, M., Kamei, N., Ehara, J., Isowa, K., and Takayama, K. (2007) A novel approach using functional peptides for efficient intestinal absorption of insulin. *J. Controlled Release*, **118**, 177–184.
94. Gomez-Icazbalceta, G., Gonzalez-Sanchez, I., Moreno, J., Cerbon, M.A., and Cervantes, A. (2013) In vitro drug metabolism testing using blood-monocyte derivatives. *Expert Opin. Drug Metab. Toxicol.*, **9**, 1571–1580.
95. Kulthong, K., Maniratanachote, R., Kobayashi, Y., Fukami, T., and Yokoi, T. (2012) Effects of silver nanoparticles on rat hepatic cytochrome P450 enzyme activity. *Xenobiotica*, **42**, 854–862.
96. Tan, J., Shah, S., Thomas, A., Ou-Yang, H.D., and Liu, Y. (2013) The influence of size, shape and vessel geometry on nanoparticle distribution. *Microfluid. Nanofluid.*, **14**, 77–87.
97. Kaminskas, L.M., Boyd, B.J., Karellas, P., Krippner, G.Y., Lessene, R., Kelly, B., and Porter, C.J. (2008) The impact of molecular weight and PEG chain length on the systemic pharmacokinetics of PEGylated poly l-lysine dendrimers. *Mol. Pharmaceutics*, **5**, 449–463.
98. Perry, J.L., Reuter, K.G., Kai, M.P., Herlihy, K.P., Jones, S.W., Luft, J.C., Napier, M., Bear, J.E., and DeSimone, J.M. (2012) PEGylated PRINT nanoparticles: the impact of PEG density on protein binding, macrophage association, biodistribution, and pharmacokinetics. *Nano Lett.*, **12**, 5304–5310.
99. Tahara, K., Miyazaki, Y., Kawashima, Y., Kreuter, J., and Yamamoto, H. (2011) Brain targeting with surface-modified poly(D,L-lactic-co-glycolic acid) nanoparticles delivered via carotid artery administration. *Eur. J. Pharm. Biopharm.*, **77**, 84–88.
100. Mudge, M.C., Walker, N.J., Borjesson, D.L., Librach, F., Johns, J.L., and Owens, S.D. (2012) Post-transfusion survival of biotin-labeled allogeneic RBCs in adult horses. *Vet. Clin. Pathol./Am. Soc. Vet. Clin. Pathol.*, **41**, 56–62.
101. Hu, C.M., Zhang, L., Aryal, S., Cheung, C., Fang, R.H., and Zhang, L. (2011) Erythrocyte membrane-camouflaged polymeric nanoparticles as a biomimetic delivery platform. *Proc. Natl. Acad. Sci. U.S.A.*, **108**, 10980–10985.
102. Manoochehri, S., Darvishi, B., Kamalinia, G., Amini, M., Fallah, M., Ostad, S.N., Atyabi, F., and Dinarvand, R. (2013) Surface modification of PLGA nanoparticles via human serum albumin conjugation for controlled delivery of docetaxel. *Daru*, **21**, 58.
103. Felmlee, M.A., Morris, M.E., and Mager, D.E. (2012) Mechanism-based pharmacodynamic modeling. *Methods Mol. Biol.*, **929**, 583–600.
104. Nielsen, E.I. and Friberg, L.E. (2013) Pharmacokinetic-pharmacodynamic modeling of antibacterial drugs. *Pharmacol. Rev.*, **65**, 1053–1090.
105. Harashima, H., Tsuchihashi, M., Iida, S., Doi, H., and Kiwada, H. (1999) Pharmacokinetic/pharmacodynamic modeling of antitumor agents encapsulated into liposomes. *Adv. Drug Delivery Rev.*, **40**, 39–61.
106. Tsuchihashi, M., Harashima, H., and Kiwada, H. (1999) Development of a pharmacokinetic/pharmacodynamic (PK/PD)-simulation system for doxorubicin in long circulating liposomes in mice using peritoneal P388. *J. Controlled Release*, **61**, 9–19.
107. Jones, H. and Rowland-Yeo, K. (2013) Basic concepts in physiologically based pharmacokinetic modeling in drug discovery and development. *CPT: Pharmacometrics Syst. Pharmacol.*, **2**, e63.
108. Li, M., Al-Jamal, K.T., Kostarelos, K., and Reineke, J. (2010) Physiologically based pharmacokinetic modeling of nanoparticles. *ACS Nano*, **4**, 6303–6317.
109. Liu, C., Krishnan, J., Stebbing, J., and Xu, X.Y. (2011) Use of mathematical models to understand anticancer drug delivery and its effect on solid tumors. *Pharmacogenomics*, **12**, 1337–1348.
110. Bachler, G., von Goetz, N., and Hungerbuhler, K. (2014) Using physiologically based pharmacokinetic (PBPK)

modeling for dietary risk assessment of titanium dioxide (TiO) nanoparticles. *Nanotoxicology*, **9**, 1–8.

111. Grassi, G., Hasa, D., Voinovich, D., Perissutti, B., Dapas, B., Farra, R., Franceschinis, E., and Grassi, M. (2010) Simultaneous release and ADME processes of poorly water-soluble drugs: mathematical modeling. *Mol. Pharmaceutics*, **7**, 1488–1497.

112. Li, M., Panagi, Z., Avgoustakis, K., and Reineke, J. (2012) Physiologically based pharmacokinetic modeling of PLGA nanoparticles with varied mPEG content. *Int. J. Nanomed.*, **7**, 1345–1356.

113. Xu, C. and Mager, D.E. (2011) Quantitative structure-pharmacokinetic relationships. *Expert Opin. Drug Metab. Toxicol.*, **7**, 63–77.

114. Trickler, W.J., Munt, D.J., Jain, N., Joshi, S.S., and Dash, A.K. (2011) Antitumor efficacy, tumor distribution and blood pharmacokinetics of chitosan/glyceryl-monooleate nanostructures containing paclitaxel. *Nanomedicine-UK*, **6**, 437–448.

115. Zhang, C., Qu, G., Sun, Y., Wu, X., Yao, Z., Guo, Q., Ding, Q., Yuan, S., Shen, Z., and Ping, Q. (2008) Pharmacokinetics, biodistribution, efficacy and safety of *N*-octyl-*O*-sulfate chitosan micelles loaded with paclitaxel. *Biomaterials*, **29**, 1233–1241.

116. Emoto, S., Yamaguchi, H., Kishikawa, J., Yamashita, H., Ishigami, H., and Kitayama, J. (2012) Antitumor effect and pharmacokinetics of intraperitoneal NK105, a nanomicellar paclitaxel formulation for peritoneal dissemination. *Cancer Sci.*, **103**, 1304–1310.

117. Kaminskas, L.M., McLeod, V.M., Kelly, B.D., Sberna, G., Boyd, B.J., Williamson, M., Owen, D.J., and Porter, C.J. (2012) A comparison of changes to doxorubicin pharmacokinetics, antitumor activity, and toxicity mediated by PEGylated dendrimer and PEGylated liposome drug delivery systems. *Nanomed. Nanotechnol. Biol. Med.*, **8**, 103–111.

118. Allen, T.M., Mumbengegwi, D.R., and Charrois, G.J. (2005) Anti-CD19-targeted liposomal doxorubicin improves the therapeutic efficacy in murine B-cell lymphoma and ameliorates the toxicity of liposomes with varying drug release rates. *Clin. Cancer Res.*, **11**, 3567–3573.

119. Chen, Z., Deng, J., Zhao, Y., and Tao, T. (2012) Cyclic RGD peptide-modified liposomal drug delivery system: enhanced cellular uptake in vitro and improved pharmacokinetics in rats. *Int. J. Nanomed.*, **7**, 3803.

120. Anders, C.K., Adamo, B., Karginova, O., Deal, A.M., Rawal, S., Darr, D., Schorzman, A., Santos, C., Bash, R., and Kafri, T. (2013) Pharmacokinetics and efficacy of PEGylated liposomal doxorubicin in an intracranial model of breast cancer. *PLoS One*, **8**, e61359.

121. Yuan, H., Chen, C.-Y., Chai, G.-h., Du, Y.-Z., and Hu, F.-Q. (2013) Improved transport and absorption through gastrointestinal tract by PEGylated solid lipid nanoparticles. *Mol. Pharmaceutics*, **10**, 1865–1873.

122. Khalil, N.M., do Nascimento, T.C.F., Casa, D.M., Dalmolin, L.F., de Mattos, A.C., Hoss, I., Romano, M.A., and Mainardes, R.M. (2013) Pharmacokinetics of curcumin-loaded PLGA and PLGA–PEG blend nanoparticles after oral administration in rats. *Colloids Surf., B*, **101**, 353–360.

123. Song, Z., Feng, R., Sun, M., Guo, C., Gao, Y., Li, L., and Zhai, G. (2011) Curcumin-loaded PLGA-PEG-PLGA triblock copolymeric micelles: preparation, pharmacokinetics and distribution in vivo. *J. Colloid Interface Sci.*, **354**, 116–123.

124. Feng, R., Song, Z., and Zhai, G. (2012) Preparation and in vivo pharmacokinetics of curcumin-loaded PCL-PEG-PCL triblock copolymeric nanoparticles. *Int. J. Nanomed.*, **7**, 4089.

125. Chou, S.-T., Leng, Q., Scaria, P., Kahn, J.D., Tricoli, L.J., Woodle, M., and Mixson, A.J. (2013) Surface-modified HK: siRNA nanoplexes with enhanced pharmacokinetics and tumor growth inhibition. *Biomacromolecules*, **14**, 752–760.

126. Sonaje, K., Lin, K.-J., Wey, S.-P., Lin, C.-K., Yeh, T.-H., Nguyen, H.-N., Hsu, C.-W., Yen, T.-C., Juang, J.-H., and Sung, H.-W. (2010) Biodistribution,

pharmacodynamics and pharmacokinetics of insulin analogues in a rat model: oral delivery using pH-responsive nanoparticles vs. subcutaneous injection. *Biomaterials*, **31**, 6849–6858.

127. Sonaje, K., Chen, Y.J., Chen, H.L., Wey, S.P., Juang, J.H., Nguyen, H.N., Hsu, C.W., Lin, K.J., and Sung, H.W. (2010) Enteric-coated capsules filled with freeze-dried chitosan/poly(gamma-glutamic acid) nanoparticles for oral insulin delivery. *Biomaterials*, **31**, 3384–3394.

128. Cheng, W.W. and Allen, T.M. (2008) Targeted delivery of anti-CD19 liposomal doxorubicin in B-cell lymphoma: a comparison of whole monoclonal antibody, Fab′ fragments and single chain Fv. *J. Controlled Release*, **126**, 50–58.

129. Ramadan, A., Lagarce, F., Tessier-Marteau, A., Thomas, O., Legras, P., Macchi, L., Saulnier, P., and Benoit, J.P. (2011) Oral fondaparinux: use of lipid nanocapsules as nanocarriers and in vivo pharmacokinetic study. *Int. J. Nanomed.*, **6**, 2941.

130. Xie, S., Zhu, L., Dong, Z., Wang, X., Wang, Y., Li, X., and Zhou, W. (2011) Preparation, characterization and pharmacokinetics of enrofloxacin-loaded solid lipid nanoparticles: influences of fatty acids. *Colloids Surf., B*, **83**, 382–387.

131. Manjunath, K. and Venkateswarlu, V. (2005) Pharmacokinetics, tissue distribution and bioavailability of clozapine solid lipid nanoparticles after intravenous and intraduodenal administration. *J. Controlled Release*, **107**, 215–228.

132. Chen, Y., Yuan, L., Zhou, L., Zhang, Z.-h., Cao, W., and Wu, Q. (2012) Effect of cell-penetrating peptide-coated nanostructured lipid carriers on the oral absorption of tripterine. *Int. J. Nanomed.*, **7**, 4581.

133. Liu, X., Liu, C., Zhang, W., Xie, C., Wei, G., and Lu, W. (2013) Oligoarginine-modified biodegradable nanoparticles improve the intestinal absorption of insulin. *Int. J. Pharm.*, **448**, 159–167.

134. Zabaleta, V., Ponchel, G., Salman, H., Agüeros, M., Vauthier, C., and Irache, J.M. (2012) Oral administration of paclitaxel with pegylated poly (anhydride) nanoparticles: permeability and pharmacokinetic study. *Eur. J. Pharm. Biopharm.*, **81**, 514–523.

135. Lecaroz, M.C., Blanco-Prieto, M.J., Campanero, M.A., Salman, H., and Gamazo, C. (2007) Poly (D, L-lactide-coglycolide) particles containing gentamicin: pharmacokinetics and pharmacodynamics in Brucella melitensis-infected mice. *Antimicrob. Agents Chemother.*, **51**, 1185–1190.

136. Milane, L., Duan, Z.-f., and Amiji, M. (2011) Pharmacokinetics and biodistribution of lonidamine/paclitaxel loaded, EGFR-targeted nanoparticles in an orthotopic animal model of multi-drug resistant breast cancer. *Nanomed. Nanotechnol. Biol. Med.*, **7**, 435–444.

137. Semete, B., Booysen, L., Lemmer, Y., Kalombo, L., Katata, L., Verschoor, J., and Swai, H.S. (2010) In vivo evaluation of the biodistribution and safety of PLGA nanoparticles as drug delivery systems. *Nanomed. Nanotechnol. Biol. Med.*, **6**, 662–671.

138. Uchino, H., Matsumura, Y., Negishi, T., Koizumi, F., Hayashi, T., Honda, T., Nishiyama, N., Kataoka, K., Naito, S., and Kakizoe, T. (2005) Cisplatin-incorporating polymeric micelles (NC-6004) can reduce nephrotoxicity and neurotoxicity of cisplatin in rats. *Br. J. Cancer*, **93**, 678–687.

139. Oberoi, H.S., Nukolova, N.V., Laquer, F.C., Poluektova, L.Y., Huang, J., Alnouti, Y., Yokohira, M., Arnold, L.L., Kabanov, A.V., and Cohen, S.M. (2012) Cisplatin-loaded core cross-linked micelles: comparative pharmacokinetics, antitumor activity, and toxicity in mice. *Int. J. Nanomed.*, **7**, 2557.

140. Chandrasekar, D., Sistla, R., Ahmad, F.J., Khar, R.K., and Diwan, P.V. (2007) The development of folate-PAMAM dendrimer conjugates for targeted delivery of anti-arthritic drugs and their pharmacokinetics and biodistribution in arthritic rats. *Biomaterials*, **28**, 504–512.

141. Dong, Z., Hamid, K.A., Gao, Y., Lin, Y., Katsumi, H., Sakane, T., and Yamamoto, A. (2011) Polyamidoamine

dendrimers can improve the pulmonary absorption of insulin and calcitonin in rats. *J. Pharm. Sci.-US*, **100**, 1866–1878.

142. Kulhari, H., Kulhari, D.P., Prajapati, S.K., and Chauhan, A.S. (2013) Pharmacokinetic and pharmacodynamic studies of poly (amidoamine) dendrimer based simvastatin oral formulations for the treatment of hypercholesterolemia. *Mol. Pharmaceutics*, **10**, 2528–2533.

143. Xiao, W., Luo, J., Jain, T., Riggs, J.W., Tseng, H.P., Henderson, P.T., Cherry, S.R., Rowland, D., and Lam, K.S. (2012) Biodistribution and pharmacokinetics of a telodendrimer micellar paclitaxel nanoformulation in a mouse xenograft model of ovarian cancer. *Int. J. Nanomed.*, **7**, 1587.

144. Zhang, H., Li, Y., Lin, T.-Y., Xiao, K., Haddad, A.S., Henderson, P.T., Jonas, B.A., Chen, M., Xiao, W., and Liu, R. (2014) Nanomicelle formulation modifies the pharmacokinetic profiles and cardiac toxicity of daunorubicin. *Nanomedicine-UK*, **20**, 1–14.

145. Kaminskas, L.M., Kelly, B.D., McLeod, V.M., Boyd, B.J., Krippner, G.Y., Williams, E.D., and Porter, C.J. (2009) Pharmacokinetics and tumor disposition of PEGylated, methotrexate conjugated poly-L-lysine dendrimers. *Mol. Pharmaceutics*, **6**, 1190–1204.

146. Hirn, S., Semmler-Behnke, M., Schleh, C., Wenk, A., Lipka, J., Schäffler, M., Takenaka, S., Möller, W., Schmid, G., and Simon, U. (2011) Particle size-dependent and surface charge-dependent biodistribution of gold nanoparticles after intravenous administration. *Eur. J. Pharm. Biopharm.*, **77**, 407–416.

147. Kirpotin, D.B., Drummond, D.C., Shao, Y., Shalaby, M.R., Hong, K., Nielsen, U.B., Marks, J.D., Benz, C.C., and Park, J.W. (2006) Antibody targeting of long-circulating lipidic nanoparticles does not increase tumor localization but does increase internalization in animal models. *Cancer Res.*, **66**, 6732–6740.

148. Han, Y., Xie, G., Sun, Z., Mu, Y., Han, S., Xiao, Y., Liu, N., Wang, H., Guo, C., and Shi, Z. (2011) Plasma kinetics and biodistribution of water-soluble CdTe quantum dots in mice: a comparison between Cd and Te. *J. Nanopart. Res.*, **13**, 5373–5380.

149. Dan, M., Wu, P., Grulke, E.A., Graham, U.M., Unrine, J.M., and Yokel, R.A. (2012) Ceria-engineered nanomaterial distribution in, and clearance from, blood: size matters. *Nanomedicine-UK*, **7**, 95–110.

150. Morais, T., Soares, M.E., Duarte, J.A., Soares, L., Maia, S., Gomes, P., Pereira, E., Fraga, S., Carmo, H., and Bastos, M.d.L. (2012) Effect of surface coating on the biodistribution profile of gold nanoparticles in the rat. *Eur. J. Pharm. Biopharm.*, **80**, 185–193.

151. Lankveld, D., Oomen, A., Krystek, P., Neigh, A., Troost–de Jong, A., Noorlander, C., Van Eijkeren, J., Geertsma, R., and De Jong, W. (2010) The kinetics of the tissue distribution of silver nanoparticles of different sizes. *Biomaterials*, **31**, 8350–8361.

152. Chu, K.S., Hasan, W., Rawal, S., Walsh, M.D., Enlow, E.M., Luft, J.C., Bridges, A.S., Kuijer, J.L., Napier, M.E., and Zamboni, W.C. (2013) Plasma, tumor and tissue pharmacokinetics of Docetaxel delivered via nanoparticles of different sizes and shapes in mice bearing SKOV-3 human ovarian carcinoma xenograft. *Nanomed. Nanotechnol. Biol. Med.*, **9**, 686–693.

153. Ganta, S., Sharma, P., Paxton, J.W., Baguley, B.C., and Garg, S. (2010) Pharmacokinetics and pharmacodynamics of chlorambucil delivered in long-circulating nanoemulsion. *J. Drug Targeting*, **18**, 125–133.

154. Tang, J., Wei, H., Liu, H., Ji, H., Dong, D., Zhu, D., and Wu, L. (2010) Pharmacokinetics and biodistribution of itraconazole in rats and mice following intravenous administration in a novel liposome formulation. *Drug Delivery*, **17**, 223–230.

155. Narayanan, S., Pavithran, M., Viswanath, A., Narayanan, D., Mohan, C.C., Manzoor, K., and Menon, D. (2014) Sequentially releasing dual-drug-loaded PLGA–casein core/shell

nanomedicine: design, synthesis, biocompatibility and pharmacokinetics. *Acta Biomater.*, **10**, 2112–2124.

156. Katragadda, U., Fan, W., Wang, Y., Teng, Q., and Tan, C. (2013) Combined delivery of paclitaxel and tanespimycin via micellar nanocarriers: pharmacokinetics, efficacy and metabolomic analysis. *PLoS One*, **8**, e58619.

157. Booysen, L., Kalombo, L., Brooks, E., Hansen, R., Gilliland, J., Gruppo, V., Lungenhofer, P., Semete-Makokotlela, B., Swai, H., and Kotze, A. (2013) *In vivo/in vitro* pharmacokinetic and pharmacodynamic study of spray-dried poly-(dl-lactic-*co*-glycolic) acid nanoparticles encapsulating rifampicin and isoniazid. *Int. J. Pharm.*, **444**, 10–17.

158. Ding, X.-Y., Hong, C.-J., Liu, Y., Gu, Z.-L., Xing, K.-L., Zhu, A.-J., Chen, W.-L., Shi, L.-S., Zhang, X.-N., and Zhang, Q. (2012) Pharmacokinetics, tissue distribution, and metabolites of a polyvinylpyrrolidone-coated norcantharidin chitosan nanoparticle formulation in rats and mice, using LC-MS/MS. *Int. J. Nanomed.*, **7**, 1723.

159. Wei, X., Senanayake, T.H., Bohling, A., and Vinogradov, S.V. (2014) Targeted nanogel conjugate for improved stability and cellular permeability of curcumin: synthesis, pharmacokinetics, and tumor growth inhibition. *Mol. Pharmaceutics*, **11**, 3112–3122.

160. Xie, S., Pan, B., Wang, M., Zhu, L., Wang, F., Dong, Z., Wang, X., and Zhou, W. (2010) Formulation, characterization and pharmacokinetics of praziquantel-loaded hydrogenated castor oil solid lipid nanoparticles. *Nanomedicine-UK*, **5**, 693–701.

161. Kim, M.-S., Jin, S.-J., Kim, J.-S., Park, H.J., Song, H.-S., Neubert, R.H., and Hwang, S.-J. (2008) Preparation, characterization and in vivo evaluation of amorphous atorvastatin calcium nanoparticles using supercritical antisolvent (SAS) process. *Eur. J. Pharm. Biopharm.*, **69**, 454–465.